Article

Late fluid flow in a primitive asteroid revealed by Lu–Hf isotopes in Ryugu

https://doi.org/10.1038/s41586-025-09483-0

Received: 7 November 2024

Accepted: 31 July 2025

Published online: 10 September 2025

Check for updates

Tsuyoshi Iizuka[1]✉, Takazo Shibuya[2], Takehito Hayakawa[3], Tetsuya Yokoyama[4], Ikshu Gautam[4], Makiko K. Haba[4], Kengo T. M. Ito[5], Yuki Hibiya[6,7], Akira Yamaguchi[8,9], Yoshinari Abe[10], Jérôme Aléon[11], Conel M. O'D. Alexander[12], Sachiko Amari[5,13], Yuri Amelin[14], Ken-ichi Bajo[15], Martin Bizzarro[16], Audrey Bouvier[17], Richard W. Carlson[12], Marc Chaussidon[18], Byeon-Gak Choi[19], Nicolas Dauphas[20,21], Andrew M. Davis[20], Tommaso Di Rocco[22], Wataru Fujiya[23], Ryota Fukai[24], Hiroshi Hidaka[25], Hisashi Homma[26], Gary R. Huss[27], Trevor R. Ireland[28], Akira Ishikawa[4], Shoichi Itoh[29], Noriyuki Kawasaki[30], Noriko T. Kita[31], Koki Kitajima[31], Thorsten Kleine[32], Shintaro Komatani[33], Alexander N. Krot[27], Ming-Chang Liu[34], Yuki Masuda[4,16], Kazuko Motomura[35], Frédéric Moynier[18], Kazuhide Nagashima[27], Izumi Nakai[36], Ann Nguyen[37], Larry Nittler[12], Andreas Pack[22], Changkun Park[38], Laurette Piani[39], Liping Qin[40], Sara Russell[41], Naoya Sakamoto[42], Maria Schönbächler[43], Lauren Tafla[34], Haolan Tang[40], Kentaro Terada[44], Yasuko Terada[45], Tomohiro Usui[24], Sohei Wada[30], Meenakshi Wadhwa[46], Richard J. Walker[47], Katsuyuki Yamashita[48], Qing-Zhu Yin[49], Shigekazu Yoneda[50], Hiroharu Yui[51], Ai-Cheng Zhang[52], Tomoki Nakamura[53], Hiroshi Naraoka[54], Takaaki Noguchi[29], Ryuji Okazaki[54], Kanako Sakamoto[24], Hikaru Yabuta[55], Masanao Abe[24], Akiko Miyazaki[24], Aiko Nakato[8,24], Masahiro Nishimura[24], Tatsuaki Okada[24], Toru Yada[24], Kasumi Yogata[24], Satoru Nakazawa[24], Takanao Saiki[24], Satoshi Tanaka[24], Fuyuto Terui[56], Yuichi Tsuda[24], Sei-ichiro Watanabe[25], Makoto Yoshikawa[24], Shogo Tachibana[24,57] & Hisayoshi Yurimoto[30]

Carbonaceous asteroids are the source of the most primitive meteorites[1] and represent leftover planetesimals that formed from ice and dust in the outer Solar System and may have delivered volatiles to the terrestrial planets[2–5]. Understanding the aqueous activity of asteroids is key to deciphering their thermal, chemical and orbital evolution, with implications for the origin of water on the terrestrial planets. Analyses of the objects, in particular pristine samples returned from asteroid Ryugu, have provided detailed information on fluid–rock interactions within a few million years after parent-body formation[6–11]. However, the long-term fate of asteroidal water remains poorly understood. Here we present evidence for fluid flow in a carbonaceous asteroid more than 1 billion years after formation, based on the ^{176}Lu–^{176}Hf decay systematics of Ryugu samples, which reflect late lutetium mobilization. Such late fluid flow was probably triggered by an impact that generated heat for ice melting and opened rock fractures for fluid migration. This contrasts the early aqueous activity powered by short-lived radioactive decay, with limited fluid flow and little elemental fractionation[12]. Our results imply that carbonaceous planetesimals accreted by the terrestrial planets could have retained not only hydrous minerals but also aqueous water, leading to an upwards revision of the inventory of their water delivery by a factor of two to three.

Carbon- and water-rich asteroids are the most abundant type in the main belt and are linked to rare and fragile carbonaceous chondritic meteorites[1]. The volatile inventory of carbonaceous asteroids was probably accreted as ice together with dust beyond the snow line in the protosolar disk[2]. Their subsequent inwards migration may have brought a significant fraction of volatiles to the terrestrial planets[2–5]. The aqueous history of carbonaceous asteroids provides clues to their thermal, chemical and orbital evolution and has implications for the origin of water on the terrestrial planets.

The Hayabusa2 spacecraft conducted in situ observations of near-Earth carbonaceous asteroid Ryugu[13,14] and collected surface and subsurface samples during the first and second touchdowns, respectively, with a total mass of 5.4 g (ref. 15). Ryugu is an approximately 1-km rubble pile formed from impact fragments sampled at various depths on a larger disrupted parent body[13,14]. Returned samples share mineralogical, chemical and isotopic characteristics with Ivuna-type (CI) chondrites, a group of meteorites that underwent the most extensive aqueous alteration but whose chemical compositions are closest to that of the solar photosphere[6–9]. In contrast to CI chondrites, however,

A list of affiliations appears at the end of the paper.

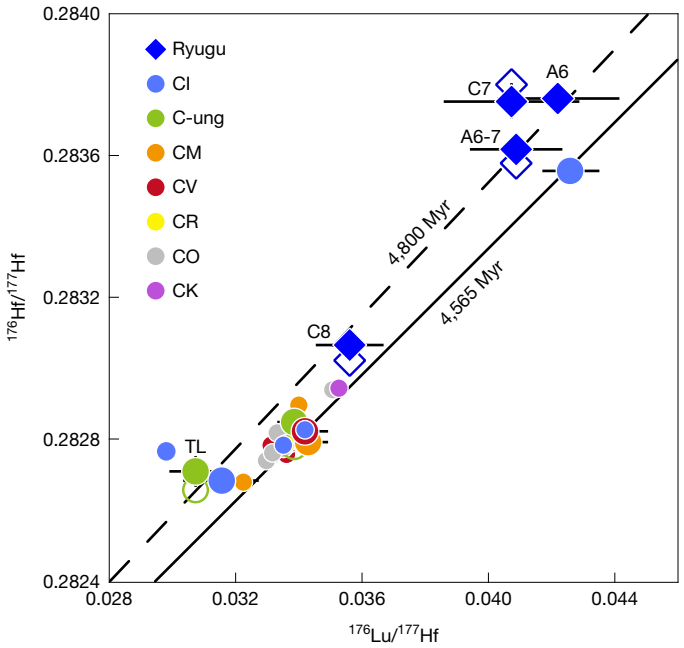

Fig. 1 | Plot of $^{176}Hf/^{177}Hf$ versus $^{176}Lu/^{177}Hf$ for Ryugu and carbonaceous chondrite samples. The data from this work and the literature[18,20–23] are represented by large and small symbols, respectively. For samples with nucleosynthetic Hf isotopic anomalies, the results without and with correction for nucleosynthetic effects are shown as open and solid symbols, respectively. Error bars plotted on our data represent the 95% confidence intervals (the bars are smaller than the symbols for $^{176}Hf/^{177}Hf$). The data are compared with reference isochrons of 4,565 Myr (solid line) and 4,800 Myr (dashed line) that go through the Solar System initial $^{176}Hf/^{177}Hf$ value of 0.279781 ± 18 defined by meteorite zircon[30]. CR, Rumuruti-type; CO, Omans-type; CK, Karoonda-type; TL, Tagish Lake; A6, A0106; A6-7, A0106-A0107; C7, C0107; C8, C0108.

Ryugu samples are almost free of ferrihydrite, sulfates and interlayer water in phyllosilicates[6–10]. These differences are probably owing to alteration of CI chondrites during their residence on Earth. Thus, Ryugu samples provide an opportunity to investigate the indigenous aqueous activity on a carbonaceous asteroid.

The results of previous studies of Ryugu samples have shown that major secondary phases such as hydrous phyllosilicates and carbonates were formed through reactions with carbon dioxide (CO_2)-bearing alkaline (about pH 10) water at about 40 °C under water-saturated conditions[6–10]. The carbonate crystallization age has been determined by the short-lived ^{53}Mn–^{53}Cr decay scheme to be within the first 7 Myr of Solar System history[7,9,11]. Early fluid activity is a consequence of the melting of accreted water (H_2O) and CO_2 ice from the heat released by the decay of ^{26}Al within the parent body[8,12]. However, little is known about the fate of water over long timescales. In this study, we present lutetium (Lu)–hafnium (Hf) isotopic data for Ryugu samples that reveal Lu transport by late fluid flow.

^{176}Lu–^{176}Hf evidence for fluid flow

The decay of ^{176}Lu to ^{176}Hf with a half-life of 37.19 Gyr (ref. 16) can be used as a chronometer and isotopic tracer for geologic processes that fractionate Lu from Hf over Solar System history[17–19]. We have measured the Lu–Hf isotopic compositions of 4 Ryugu aggregate samples of <1 mm particles, with an integrated mass of approximately 20 mg for each aggregate: A0106 and A0106-A0107 from the first touchdown site and C0107 and C0108 from the second site, which is covered with ejecta excavated from a depth of approximately 1 m by an artificial impact[15]. A0106-A0107 and C0108 were pristine samples, whereas A0106 and C0107 were processed for soluble organic matter (SOM) extraction using hexane, dichloromethane, methanol and water before acid sample digestion. We have also analysed similar amounts of six carbonaceous chondrites: CI chondrites Orgueil and Alais, Mighei-type (CM) chondrite Murchison, Vigarano-type (CV) chondrite Allende, and ungrouped (C-ung) chondrites Tagish Lake and Tarda. The Lu–Hf isotopic measurements were performed by inductively coupled plasma mass spectrometry (Methods).

The Ryugu and carbonaceous chondrite samples show a wide range of $^{176}Lu/^{177}Hf$ and $^{176}Hf/^{177}Hf$ compared with previously analysed carbonaceous chondrites with larger sample sizes ($^{176}Lu/^{177}Hf$ = 0.0337 ± 17 and $^{176}Hf/^{177}Hf$ = 0.282809 ± 98, 2 s.d. (refs. 18,20–23; Fig. 1 and Extended Data Table 1). In particular, our Orgueil and 3 Ryugu samples have remarkably high $^{176}Lu/^{177}Hf$ and $^{176}Hf/^{177}Hf$ values of 0.0408–0.0426 and 0.283558–0.283802, respectively. The wide range of $^{176}Lu/^{177}Hf$ and $^{176}Hf/^{177}Hf$ is most probably owing to the heterogeneous distribution of accessory apatite ($Ca_5(PO_4)_3(F,Cl,OH)$), which is the major carrier of rare earth elements (REEs)[7,8,24,25]. In fact, the abundance of apatite significantly varies in Orgueil and Ryugu clasts[7,10,25]. The Lu–Hf data points for all carbonaceous chondrites, except for Tagish Lake, plot on a reference isochron of 4,565 Myr, which is the approximate age of the accretion of their parent bodies[8,26]. In contrast, Ryugu samples plot above the reference isochron beyond analytical uncertainty. The observed shifts from the isochron are equivalent to ^{176}Hf excesses up to about 10 parts per ten thousand (ε units) at a given $^{176}Lu/^{177}Hf$ or alternatively to Lu deficits up to about 5% at a given $^{176}Hf/^{177}Hf$.

Similar ^{176}Hf excesses or Lu deficits have been found in a number of non-carbonaceous meteorites[19,23,27], and four possible origins have been considered: (1) accelerated decay of ^{176}Lu, (2) nucleosynthetic heterogeneity, (3) reactions with cosmogenic neutrons, and (4) secondary disturbances.

The ^{176}Lu–^{176}Hf decay can be accelerated via excitation of the ^{176}Lu ground state to its short-lived isomer with a half-life of 3.7 h (refs. 28,29). Accelerated ^{176}Lu decay accounting for a 10 ε excess of ^{176}Hf should be accompanied by a 7‰ decrease in $^{176}Lu/^{175}Lu$. However, all $^{176}Lu/^{175}Lu$ values obtained for our samples are identical within the range of 0.4‰ to values reported for non-irradiated terrestrial and meteoritic basalts[30,31] (Extended Data Table 2), eliminating this possibility.

The Ryugu and ungrouped carbonaceous chondrite samples have correlated anomalies in $\varepsilon^{180}Hf$ and $\varepsilon^{178}Hf$ (Fig. 2). Similar correlated $\varepsilon^{180}Hf$–$\varepsilon^{178}Hf$ variations were observed in refractory inclusions, acid leachates and residues of carbonaceous chondrites, and were attributed to heterogeneous contributions of presolar grains carrying Hf produced by the slow neutron-capture process (s-process)[32,33]. Our results reveal that the most primitive carbonaceous samples preserved nucleosynthetic heterogeneity, even on an approximately 20-mg whole-rock scale. Nucleosynthetic effects on $^{176}Hf/^{177}Hf$ can be corrected using the theoretically predicted correlation between Hf isotopic ratios[34] (Methods). The corrections change $^{176}Hf/^{177}Hf$ by −1.7 ε to +2.5 ε (Extended Data Table 1), leaving excess ^{176}Hf in all Ryugu samples and Tagish Lake unexplained (Fig. 1).

Some of our Ryugu and chondrite samples show resolvable deficits in ^{149}Sm caused by cosmogenic neutron capture[35]. Neutron capture, particularly that in the epithermal energy range, raises $^{176}Hf/^{177}Hf$ and $\varepsilon^{178}Hf$ and lowers $\varepsilon^{180}Hf$ (Methods). Although both samarium (Sm) and Hf in returned lunar samples show isotopic variations arising from thermal and epithermal neutron-capture reactions[36], our Hf isotopic data show no detectable cosmogenic effects (Fig. 2). The combined Hf–Sm isotope systematics indicate that the fluences of thermal and epithermal neutrons on the Ryugu samples are as high as 3×10^{15} n cm^{-2} and less than 8×10^{15} n cm^{-2}, respectively (Methods and Extended Data Fig. 1). Under these neutron-fluence conditions, cosmogenic ^{176}Hf excess of no more than 1 ε can be accommodated (Methods and Extended Data Fig. 2).

Apparent ^{176}Hf excess can be produced in a sample when its Lu/Hf decreases after significant accumulation of radiogenic ^{176}Hf (Extended Data Fig. 3). The apparent ^{176}Hf excesses observed in some meteorites

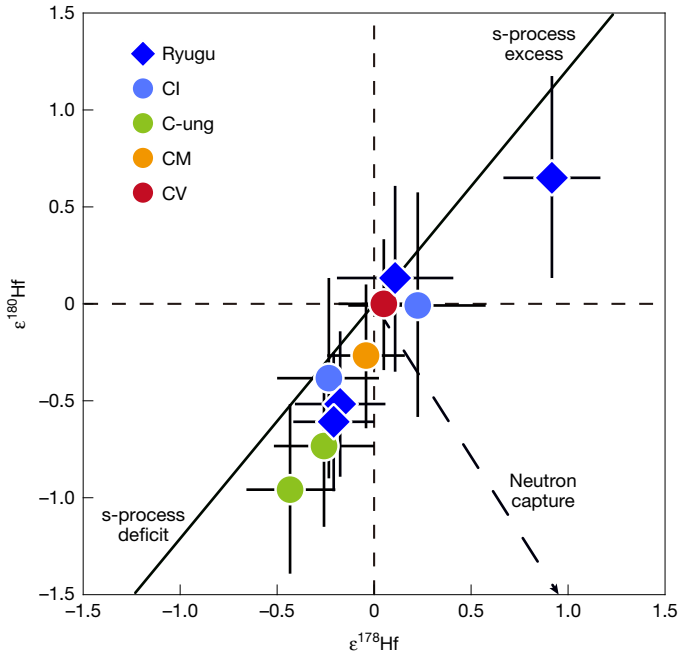

Fig. 2 | Non-radiogenic Hf isotopic composition of Ryugu and carbonaceous chondrite samples. The solid line represents the Hf isotopic variation arising from the heterogeneous distribution of an s-process component[34]. The dashed arrow indicates Hf isotopic shift due to secondary neutron-capture reactions[36]. Error bars represent the 95% confidence intervals.

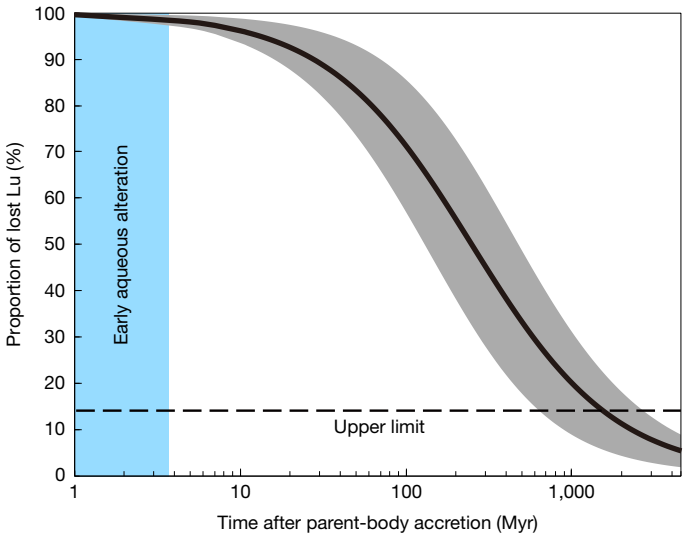

Fig. 3 | Timing and extent of Lu loss to produce apparent excess ^{176}Hf. The proportion of lost Lu (p) needed to account for the apparent ^{176}Hf excess in the pristine Ryugu sample A0106-A0107 (after correction for nucleosynthetic effects), depending on the time interval from parent-body accretion to Lu loss (Δt). The solid line and grey band represent the mean and 95% confidence interval, respectively. The light blue area indicates the period of early aqueous alteration and the horizontal dashed line denotes the upper limit of p for the sample.

were attributed to the preferential loss of Lu over Hf through diffusion during high-temperature metamorphism on the parent bodies[37,38] or through reactions with fluids during terrestrial weathering[39,40]. They can also be caused by terrestrial contamination[41]. However, samples directly returned from Ryugu would have resided at temperatures below about 100 °C since their formation[8,9], conditions under which solid-state diffusion and vaporization of Lu and Hf are negligible. Although two of the four Ryugu samples were processed for the SOM extraction before Lu–Hf isotopic analysis, independent tests using Orgueil and Tarda show that its effect on the Lu–Hf system is limited (Extended Data Table 3). Overall, the only plausible explanation for the deviations of all Ryugu samples from the reference isochron is secondary Lu removal by fluid flow on Ryugu or its parent body.

Mechanism and timing of Lu loss

Using the apparent excess ^{176}Hf as a tracer and combined with previously reported data for Ryugu samples, we explore the mechanism and timing of Lu loss. The degree of apparent ^{176}Hf excess in a sample relative to the 4,565-Myr reference isochron (Fig. 1) depends on the extent and timing of Lu loss:

$$\Delta\left(\frac{^{176}\mathrm{Hf}}{^{177}\mathrm{Hf}}\right)_{\mathrm{sample}} = \frac{p}{1-p}\left(\frac{^{176}\mathrm{Lu}}{^{177}\mathrm{Hf}}\right)_{\mathrm{sample}}\left[\mathrm{e}^{\lambda t_0} - \mathrm{e}^{\lambda(t_0-\Delta t)}\right], \quad (1)$$

where $\lambda = 1.864 \times 10^{-11}$ yr^{-1} (ref. 16) is the decay constant of ^{176}Lu, p is the proportion of lost Lu to the total Lu in the sample, t_0 is the accretion age of the parent body about 4,565 Myr ago[8], and Δt is the time interval from parent-body accretion to Lu loss (Extended Data Fig. 3). Smaller values of Δt require large values of p to account for the observed Δ^{176}Hf/^{177}Hf in a sample (Fig. 3 and Extended Data Fig. 4). Even in the case of recent Lu loss, about 5% of Lu needs to be lost from Ryugu samples. Compared with alkali elements such as sodium (Na) and lithium (Li), Lu is rather insoluble in aqueous fluids that react with common terrestrial rocks. Although Ryugu samples processed for the SOM extraction and Tagish Lake show remarkable depletion in these soluble elements, pristine Ryugu samples do not (Extended Data Fig. 5). This demands a process that preferentially mobilized Lu in Ryugu samples. Independent lines of mineralogical evidence suggest that this Lu mobilization was caused by the flow of fluids that dissolved apatite.

In Ryugu fragments and CI chondrites, apatite hosts the majority of the total REE budget and is closely associated with carbonate and magnetite, indicating their paragenesis during early aqueous alteration[8,24]. Ryugu apatite often exhibits grain-boundary corrosion, reflecting its partial dissolution by fluids during a later alteration episode[10,24]. The fluids were probably enriched in the constituent elements of apatite as well as in alkali elements. In addition, late circulation of the fluids is indicated by the occurrence of amorphous Na–magnesium (Mg) phosphates in the rare least-altered Ryugu fragments. Notably, Na–Mg phosphates occur as veins that cross-cut brecciated fabrics of altered lithology, demonstrating their formation after early alteration and impact events[10]. They sometimes contain voids owing to vaporization during their formation[8]. These observations suggest that amorphous Na–Mg phosphates precipitated from alkali–phosphorous (P)-rich fluids as the result of water consumption through the hydration of primitive silicates and the oxidation of reduced phases associated with hydrogen (H_2) degassing. This process probably occurred during fluid migration in the shallow zone of the Ryugu parent body, where early aqueous alteration was limited by the restricted temperature increase. We expect that Na–Mg phosphates precipitated in the shallow zone are enriched in Lu and have apparent ^{176}Hf deficits complementary to the excesses observed in our samples that would originate mainly from a deeper Lu-depleted zone of the parent body.

The earliest possible timing of Lu transport by fluids can be estimated from the probable range of the original Lu abundance in each sample. Despite the expected secondary Lu loss via apatite dissolution, current abundances of REEs and P in the Ryugu samples are comparable to or even higher than the mean CI chondrite abundances (Extended Data Fig. 5 and Extended Data Table 4). Our Orgueil sample is also enriched in REEs and P relative to mean CI chondrites. These REE-P enrichments are probably due to the sampling of apatite-rich lithology in our Ryugu

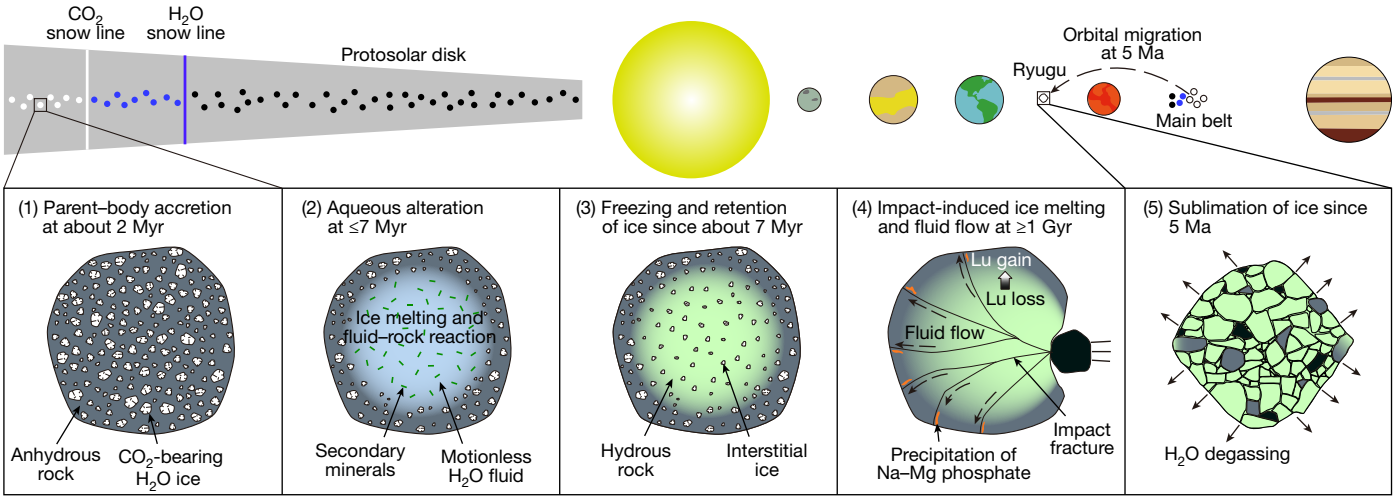

Fig. 4 | Schematic of the aqueous activity on Ryugu and its parent body. (1) The Ryugu parent body accreted from ice and dust in the outer protosolar disk at about 2 Myr after Solar System formation[8]. (2) Ice melting by short-lived radioactive heating induced early aqueous alteration under water-saturated and isochemical conditions at ≤7 Myr (refs. 7,9,11). (3) The saturated water refroze upon cooling, forming interstitial ice. (4) More than 1 Gyr later, an impact generated heat for melting of interstitial ice and rock fractures for fluid pathways, resulting in a limited escape of fluid. (5) Ryugu migrated from the main belt to the near-Earth orbit about 5 Ma (refs. 51,52) and has significantly degassed water through ice sublimation and vapour diffusion since then.

and Orgueil fragments[42]. The dispersion of the elemental abundance arising from such a nugget effect can be estimated as a function of the sample mass if the nugget abundance, composition and size are known[43]. Assuming that CI chondrites[25] are a reasonable analogue of Ryugu fragments before apatite dissolution, the 95% confidence interval of the original Lu abundance can be estimated to be between 0.0156 μg g^{-1} and 0.0398 μg g^{-1} for Ryugu A0106-A0107 (Methods). This allowable range, combined with the current Lu abundance in the sample, constrains the proportion of lost Lu to be less than 14%, which in turn sets a lower bound of 10^3 Myr for Δt (Fig. 3; see similar results for the other Ryugu samples in Extended Data Fig. 4). This age constraint is concordant with the rhenium (Re)–osmium (Os) isotopic data for Ryugu samples showing Re/Os fractionation within the past 2 Gyr (ref. 7), although Re/Os fractionation can occur during volatilization rather than during fluid flow[44].

In a recent uranium (U)-series study[45], $^{234}U/^{238}U$ and $^{238}U/^{230}Th$ higher than the secular equilibrium values were obtained from all analysed carbonaceous chondrites, among which Tagish Lake showed the largest disequilibrium. The disequilibria demonstrate that these chondrites underwent U isotopic and thorium (Th)/U fractionations within the past few 100,000 years, probably owing to the fluid transport of U. However, it remains unclear whether the fluid was generated by the breakdown of phyllosilicates or the melting of frozen aqueous water. In addition, some carbonaceous chondrites may have been exposed to water after fall on Earth. Because phyllosilicates in returned Ryugu samples remain intact[9], our results provide evidence for the late flow of aqueous fluid generated by the melting of ice on a carbonaceous asteroid.

Fate of water in carbonaceous asteroids

The solar-like chemical compositions of CI chondrites except for volatile elements have long been taken as evidence of isochemical alteration by static aqueous fluids[46]. The lack of fluid motion can be attributed to the small parent-body size (<50 km; refs. 12,47) or to the low permeability of carbonaceous chondritic rock (≤10^{-17} m^2; ref. 48). However, the mineral assemblage and depletion of interlayer water in Ryugu samples indicate that they were initially altered in the presence of excess water, but the water was largely lost at some point[8,9]. This is also the case for CI chondrites if their interlayer water is of terrestrial origin[12,49].

By revealing secondary Lu removal from Ryugu samples by fluids, our study suggests that they retained ice over a billion-year timescale and then underwent one or more events that caused melting of the ice and fluid flow (Fig. 4). Potential heat sources for melting ice at such a late time are (1) solar radiation at perihelion of Ryugu and (2) impacts on Ryugu and/or its parent body. We favour impact heating on the Ryugu parent body. Fluid generation by solar heating is viable only at depths of <40 cm on near-Earth objects[50]. However, both surface and subsurface Ryugu samples record secondary Lu loss, the latter of which would have resided at a depth of about 1 m since Ryugu migrated from the main belt to near-Earth orbit approximately 5 million years ago (Ma)[51,52]. The occurrence of Na–Mg phosphate veins in the least-altered Ryugu fragments suggests that fluids flowed from the interior to the shallow zone of the Ryugu parent body. Moreover, impacts would fracture rocks and increase the effective permeability, thereby providing an explanation as to why fluids were static during early aqueous alteration but mobilized later. Nonetheless, the impact-induced fluid flow should not be too pervasive, otherwise we cannot explain the rarity of the veins and the lack of highly soluble element depletion in pristine Ryugu samples. The preservation of solar-like elemental abundances despite the loss of excess water is explained if the water primarily escaped by degassing rather than by fluid exhalation. Conceivably, the near-surface degassing of icy objects is a natural outcome of their inwards orbital migration that enhances the sublimation of ice and the transport of vapour through fractures and pores. Applying pore diameters of the order of 1 μm (ref. 7) and an effective permeability of 10^{-15} m^2, the ice sublimation and vapour diffusion model of ref. 53 predicts water degassing to a depth of 10^2 m on Ryugu for about 5 Myr. This scenario is consistent with the presence of ice on the surface of the carbonaceous asteroid Themis in the outer main belt[54,55].

The implication of Ryugu's aqueous history (Fig. 4) is that CI chondrite-like planetesimals accreted by the terrestrial planets could preserve both structural OH in hydrous minerals and (frozen) aqueous water, unless they were small (≤10^2 m) objects. Considering an initial water–rock mass ratio of 0.3–0.5 that reproduces the typical mineral assemblages of Ryugu and CI chondrites, the combined mass fraction of structural OH and aqueous fluid in the rock–fluid system would range from 20 wt% to 30 wt% (Methods and Extended Data Fig. 6). This water abundance is higher than the water inventory of about 10 wt% commonly used for the carbonaceous building blocks of the terrestrial planets[4,5].

Online content

Any methods, additional references, Nature Portfolio reporting summaries, source data, extended data, supplementary information, acknowledgements, peer review information; details of author contributions and competing interests; and statements of data and code availability are available at https://doi.org/10.1038/s41586-025-09483-0.

1. DeMeo, F. E. et al. Connecting asteroids and meteorites with visible and near-infrared spectroscopy. *Icarus* **380**, 114971 (2022).
2. Trigo-Rodríguez, J. M., Rimola, A., Tanbakouei, S., Soto, V. C. & Lee, M. Accretion of water in carbonaceous chondrites: current evidence and implications for the delivery of water to early Earth. *Space Sci. Rev.* **215**, 18 (2019).
3. Alexander, C. M. O. 'D. et al. The provenances of asteroids, and their contributions to the volatile inventories of the terrestrial planets. *Science* **337**, 721–723 (2012).
4. Morbidelli, A., Lunine, J. I., O'Brien, D. P., Raymond, S. N. & Walsh, K. J. Building terrestrial planets. *Ann. Rev. Earth Planet. Sci.* **40**, 251–275 (2012).
5. McCubbin, F. M. & Barnes, J. J. Origin and abundances of H_2O in the terrestrial planets, Moon, and asteroids. *Earth Planet. Sci. Lett.* **526**, 115771 (2019).
6. Ito, M. et al. A pristine record of outer Solar System materials from asteroid Ryugu's returned sample. *Nat. Astron.* **6**, 1163–1171 (2022).
7. Nakamura, E. et al. On the origin and evolution of the asteroid Ryugu: a comprehensive geochemical perspective. *Proc. Jpn Acad. Ser. B* **98**, 227–282 (2022).
8. Nakamura, T. et al. Formation and evolution of carbonaceous asteroid Ryugu: direct evidence from returned samples. *Science* **379**, eabn8671 (2022).
9. Yokoyama, T. et al. Samples returned from the asteroid Ryugu are similar to Ivuna-type carbonaceous meteorites. *Science* **379**, eabn7850 (2022).
10. Yamaguchi, A. et al. Insight into multi-step geological evolution of C-type asteroids from Ryugu particles. *Nat. Astron.* **7**, 398–405 (2023).
11. McCain, K. A. et al. Early fluid activity on Ryugu inferred by isotopic analyses of carbonates and magnetite. *Nat. Astron.* **7**, 309–317 (2023).
12. Tang, H. et al. The oxygen isotopic composition of samples returned from asteroid Ryugu with implications for the nature of the parent planetesimal. *Planet. Sci. J.* **4**, 144 (2023).
13. Sugita, S. et al. The geomorphology, color, and thermal properties of Ryugu: implications for parent-body processes. *Science* **364**, eaaw0422 (2019).
14. Watanabe, S. et al. Hayabusa2 arrives at the carbonaceous asteroid 162173 Ryugu—a spinning top-shaped rubble pile. *Science* **364**, 268–272 (2019).
15. Tachibana, S. et al. Pebbles and sand on asteroid (162173) Ryugu: in situ observation and particles returned to Earth. *Science* **375**, 1011–1016 (2022).
16. Hayakawa, T., Shizuma, T. & Iizuka, T. Half-life of the nuclear cosmochronometer ^{176}Lu measured with a windowless 4π solid angle scintillation detector. *Commun. Phys.* **6**, 299 (2023).
17. Patchett, P. J., Kouvo, O., Hedge, C. E. & Tatsumoto, M. Evolution of continental crust and mantle heterogeneity: evidence from Hf isotopes. *Contrib. Mineral. Petrol.* **78**, 279–297 (1981).
18. Blichert-Toft, J. & Albarède, F. The Lu–Hf isotope geochemistry of chondrites and the evolution of the mantle–crust system. *Earth Planet. Sci. Lett.* **148**, 243–258 (1997).
19. Scherer, E., Cameron, K. L. & Blichert-Toft, J. Lu–Hf garnet geochronology: closure temperature relative to the Sm–Nd system and the effects of trace mineral inclusions. *Geochim. Cosmochim. Acta* **64**, 3413–3432 (2000).
20. Bizzarro, M., Baker, J. A., Haack, H., Ulfbeck, D. & Rosing, M. Early history of Earth's crust–mantle system inferred from hafnium isotopes in chondrites. *Nature* **421**, 931–933 (2003).
21. Patchett, P. J., Vervoort, J. D., Söderlund, U. & Salters, V. J. Lu–Hf and Sm–Nd isotopic systematics in chondrites and their constraints on the Lu–Hf properties of the Earth. *Earth Planet. Sci. Lett.* **222**, 29–41 (2004).
22. Bouvier, A., Vervoort, J. D. & Patchett, P. J. The Lu–Hf and Sm–Nd isotopic composition of CHUR: constraints from unequilibrated chondrites and implications for the bulk composition of terrestrial planets. *Earth Planet. Sci. Lett.* **273**, 48–57 (2008).
23. Dauphas, N. & Pourmand, A. Hf–W–Th evidence for rapid growth of Mars and its status as a planetary embryo. *Nature* **473**, 489–492 (2011).
24. Tkalcec, B. J. et al. A comprehensive study of apatite grains in Ryugu rock fragments. *Meteorit. Planet. Sci.* **59**, 2149–2165 (2024).
25. Morlok, A. et al. Brecciation and chemical heterogeneities of CI chondrites. *Geochim. Cosmochim. Acta* **70**, 5371–5394 (2006).
26. Iizuka, T., Hibiya, Y., Yoshihara, S. & Hayakawa, T. Timescales of solar system formation based on Al–Ti isotope correlation by supernova ejecta. *Astrophys. J. Lett.* **979**, L29 (2025).
27. Bizzarro, M., Connelly, J. N., Thrane, K. & Borg, L. E. Excess hafnium-176 in meteorites and the early Earth zircon record. *Geochem. Geophys. Geosyst.* **13**, Q03002 (2012).
28. Albarède, F. et al. γ-ray irradiation in the early Solar System and the conundrum of the ^{176}Lu decay constant. *Geochim. Cosmochim. Acta* **70**, 1261–1270 (2006).
29. Thrane, K., Connelly, J. N., Bizzarro, M. & Meyer, B. S. Origin of excess ^{176}Hf in meteorites. *Astrophys. J.* **717**, 861–867 (2010).
30. Iizuka, T., Yamaguchi, T., Hibiya, Y. & Amelin, Y. Meteorite zircon constraints on the bulk Lu–Hf isotope composition and early differentiation of the Earth. *Proc. Natl Acad. Sci. USA* **112**, 5331–5336 (2015).
31. Wimpenny, J., Amelin, Y. & Yin, Q.-Z. The Lu isotopic composition of achondrites: closing the case for accelerated decay of ^{176}Lu. *Astrophys. J. Lett.* **812**, L3 (2015).
32. Yin, Q.-Z., Lee, C. T. A. & Ott, U. Signatures of the s-process in presolar silicon carbide grains: barium through hafnium. *Astrophy. J.* **647**, 676–684 (2006).
33. Qin, L., Carlson, R. W. & Alexander, C. M. O. 'D. Correlated nucleosynthetic isotopic variability in Cr, Sr, Ba, Sm, Nd and Hf in Murchison and QUE 97008. *Geochim. Cosmochim. Acta* **75**, 7806–7828 (2011).
34. Bisterzo, S., Gallino, R., Straniero, O., Cristallo, S. & Käppeler, F. The s-process in low-metallicity stars–II. Interpretation of high-resolution spectroscopic observations with asymptotic giant branch models. *Mon. Not. R. Astron. Soc.* **418**, 284–319 (2011).
35. Torrano, Z. A. et al. Neodymium-142 deficits and samarium neutron stratigraphy of C-type asteroid (162173) Ryugu. *Meteorit. Planet. Sci.* **59**, 1966–1982 (2024).
36. Sprung, P., Kleine, T. & Scherer, E. E. Isotopic evidence for chondritic Lu/Hf and Sm/Nd of the Moon. *Earth Planet. Sci. Lett.* **380**, 77–87 (2013).
37. Bloch, E., Watkins, J. & Ganguly, J. Diffusion kinetics of lutetium in diopside and the effect of thermal metamorphism on Lu–Hf systematics in clinopyroxene. *Geochim. Cosmochim. Acta* **204**, 32–51 (2017).
38. Debaille, V., Van Orman, J., Yin, Q.-Z. & Amelin, Y. The role of phosphates for the Lu–Hf chronology of meteorites. *Earth Planet. Sci. Lett.* **473**, 52–61 (2017).
39. Bast, R. et al. Reconciliation of the excess ^{176}Hf conundrum in meteorites: recent disturbances of the Lu–Hf and Sm–Nd isotope systematics. *Geochim. Cosmochim. Acta* **212**, 303–323 (2017).
40. Maeda, R. et al. The effects of Antarctic alteration and sample heterogeneity on Sm–Nd and Lu–Hf systematics in H chondrites. *Geochim. Cosmochim. Acta* **305**, 106–129 (2021).
41. Bast, R., Scherer, E. E. & Bischoff, A. The ^{176}Lu–^{176}Hf systematics of ALM-A: a sample of the recent Almahata Sitta meteorite fall. *Geochem. Persp. Lett.* **3**, 45–54 (2017).
42. Yokoyama, T. et al. The elemental abundances of Ryugu: assessment of chemical heterogeneities and the nugget effect. *Geochem. J.* **59**, 45–63 (2025).
43. Dauphas, N. & Pourmand, A. Thulium anomalies and rare earth element patterns in meteorites and Earth: nebular fractionation and the nugget effect. *Geochim. Cosmochim. Acta* **163**, 234–261 (2015).
44. Ota, T. et al. The formation of a rubble pile asteroid: Insights from the asteroid Ryugu. *Universe* **9**, 293 (2023).
45. Turner, S., McGee, L., Humayun, M., Creech, J. & Zanda, B. Carbonaceous chondrite meteorites experienced fluid flow within the past million years. *Science* **371**, 164–167 (2021).
46. McSween, H. Y. Jr Are carbonaceous chondrites primitive or processed? A review. *Rev. Geophys.* **17**, 1059–1078 (1979).
47. Young, E. D., Zhang, K. K. & Schubert, G. Conditions for pore water convection within carbonaceous chondrite parent bodies—implications for planetesimal size and heat production. *Earth Planet. Sci. Lett.* **213**, 249–259 (2003).
48. Bland, P. A. et al. Why aqueous alteration in asteroids was isochemical: high porosity ≠ high permeability. *Earth Planet. Sci. Lett.* **287**, 559–568 (2009).
49. Vacher, L. G. et al. Hydrogen in chondrites: influence of parent body alteration and atmospheric contamination on primordial components. *Geochim. Cosmochim. Acta* **281**, 53–66 (2020).
50. Suttle, M. D., Folco, L., Genge, M. J. & Russell, S. S. Flying too close to the Sun—the viability of perihelion-induced aqueous alteration on periodic comets. *Icarus* **351**, 113956 (2020).
51. Nishiizumi, K. et al. Exposure conditions of samples collected on Ryugu's two touchdown sites determined by cosmogenic nuclides ^{10}Be and ^{26}Al. In *53rd Lunar and Planetary Science Conference* 1777 (2022).
52. Okazaki, R. et al. Noble gases and nitrogen in samples of asteroid Ryugu record its volatile sources and recent surface evolution. *Science* **379**, eabo0431 (2022).
53. Grimm, R. E. & McSween, H. Y. Jr Water and the thermal evolution of carbonaceous chondrite parent bodies. *Icarus* **82**, 244–280 (1989).
54. Campins, H. et al. Water ice and organics on the surface of the asteroid 24 Themis. *Nature* **464**, 1320–1321 (2010).
55. Rivkin, A. S. & Emery, J. P. Detection of ice and organics on an asteroidal surface. *Nature* **464**, 1322–1323 (2010).

[1]Department of Earth and Planetary Science, The University of Tokyo, Tokyo, Japan. [2]Institute for Extra-cutting-edge Science and Technology Avant-garde Research (X-star), Japan Agency for Marine-Earth Science and Technology (JAMSTEC), Kanagawa, Japan. [3]Kansai Institute for Photon Science, National Institutes for Quantum Science and Technology, Kyoto, Japan. [4]Department of Earth and Planetary Sciences, Institute of Science Tokyo, Tokyo, Japan. [5]Geochemical Research Center, The University of Tokyo, Tokyo, Japan. [6]Research Center for Advanced Science and Technology, The University of Tokyo, Tokyo, Japan. [7]Submarine Resources Research Center, JAMSTEC, Kanagawa, Japan. [8]National Institute of Polar Research, Tokyo, Japan. [9]The Graduate University for Advanced Studies (SOKENDAI), Hayama, Japan. [10]Department of Applied Chemistry, School of Engineering, Tokyo Denki University, Tokyo, Japan. [11]Institut de Minéralogie, de Physique des Matériaux et de Cosmochimie, Sorbonne Université, Museum National d'Histoire Naturelle, CNRS UMR 7590, IRD, Paris, France. [12]Earth and Planets Laboratory, Carnegie Institution for Science, Washington DC, USA. [13]McDonnell Center for the Space Sciences and Physics Department, Washington University, St. Louis, MO, USA. [14]Division of Earth and Environmental Sciences, Korea Basic Science Institute, Chungbuk, Republic of Korea. [15]Department of Earth and Planetary Sciences, Hokkaido University, Sapporo, Japan. [16]Centre for Star and Planet Formation, GLOBE Institute, University of Copenhagen, Copenhagen, Denmark. [17]Bayerisches Geoinstitut, Universität Bayreuth, Bayreuth, Germany. [18]Université Paris Cité, Institut de physique du globe de Paris,

CNRS, Paris, France. [19]Department of Earth Science Education, Seoul National University, Seoul, Republic of Korea. [20]Department of the Geophysical Sciences and Enrico Fermi Institute, The University of Chicago, Chicago, IL, USA. [21]Origins Laboratory, Department of Earth and Planetary Sciences, The University of Hong Kong, Hong Kong SAR, China. [22]Faculty of Geosciences and Geography, University of Göttingen, Göttingen, Germany. [23]Faculty of Science, Ibaraki University, Mito, Japan. [24]ISAS, JAXA, Sagamihara, Japan. [25]Earth and Planetary Sciences, Nagoya University, Nagoya, Japan. [26]Osaka Application Laboratory, SBUWDX, Rigaku Corporation, Osaka, Japan. [27]Hawai'i Institute of Geophysics and Planetology, University of Hawai'i at Mānoa, Honolulu, HI, USA. [28]School of Earth and Environmental Sciences, The University of Queensland, St Lucia, Queensland, Australia. [29]Earth and Planetary Sciences, Kyoto University, Kyoto, Japan. [30]Natural History Sciences, IIL, Hokkaido University, Sapporo, Japan. [31]Geoscience, University of Wisconsin-Madison, Madison, WI, USA. [32]Max Planck Institute for Solar System Research, Göttingen, Germany. [33]Analytical Technology, Horiba Techno Service Co. Ltd, Kyoto, Japan. [34]Earth, Planetary, and Space Sciences, UCLA, Los Angeles, CA, USA. [35]Thermal Analysis, Rigaku Corporation, Tokyo, Japan. [36]Applied Chemistry, Tokyo University of Science, Tokyo, Japan. [37]Astromaterials Research and Exploration Science, NASA Johnson Space Center, Houston, TX, USA. [38]Earth-System Sciences, Korea Polar Research Institute, Incheon, Korea. [39]Centre de Recherches Pétrographiques et Géochimiques, CNRS - Université de Lorraine, Nancy, France. [40]CAS Key Laboratory of Crust-Mantle Materials and Environments, School of Earth and Space Sciences, University of Science and Technology of China, Hefei, China. [41]Department of Earth Sciences, Natural History Museum, London, UK. [42]Isotope Imaging Laboratory, Creative Research Institution, Hokkaido University, Sapporo, Japan. [43]Institute for Geochemistry and Petrology, Department of Earth Sciences, ETH Zurich, Zurich, Switzerland. [44]Earth and Space Science, Osaka University, Osaka, Japan. [45]Spectroscopy and Imaging, Japan Synchrotron Radiation Research Institute, Hyogo, Japan. [46]School of Earth and Space Exploration, Arizona State University, Tempe, AZ, USA. [47]Geology, University of Maryland, College Park, MD, USA. [48]Graduate School of Environmental, Life, Natural Science and Technology, Okayama University, Okayama, Japan. [49]Earth and Planetary Sciences, University of California, Davis, Davis, CA, USA. [50]Science and Engineering, National Museum of Nature and Science, Tsukuba, Japan. [51]Chemistry, Tokyo University of Science, Tokyo, Japan. [52]School of Earth Sciences and Engineering, Nanjing University, Nanjing, China. [53]Department of Earth Science, Tohoku University, Sendai, Japan. [54]Department of Earth and Planetary Sciences, Kyushu University, Fukuoka, Japan. [55]Earth and Planetary Systems Science Program, Hiroshima University, Higashi-Hiroshima, Japan. [56]Kanagawa Institute of Technology, Atsugi, Japan. [57]UTokyo Organization for Planetary and Space Science, The University of Tokyo, Tokyo, Japan. ✉e-mail: iizuka@eps.s.u-tokyo.ac.jp

Methods

Samples and sample preparation

Ryugu fragments sampled during the first and second touchdown operations were stored in the chambers A and C of the Hayabusa2 spacecraft, respectively. Although both sampling operations were made on the surface, chamber C samples include subsurface material excavated from a depth of approximately 1 m below the surface by an impact experiment near the second touchdown site[15,56]. The Ryugu samples analysed in this study were taken from four aggregates of <1-mm particles catalogued as A0106, A0107, C0107 and C0108 with total masses of 38.4 mg, 31.0 mg, 38.8 mg and 33.0 mg, respectively. A0106 and A0107 were from the chamber A and C0107 and C0108 were from the chamber C. Sample A0106-A0107 was a powdered material from a combined aggregate of 1.6 mg A0106 and 27 mg A0107, among which a 23.88-mg aliquot was digested for a series of studies of the inorganic chemical and isotopic compositions by the Hayabusa2-initial-analysis chemistry team, including the present work. Sample C0108 was powdered from a 33.3-mg aggregate, and a 22.24-mg aliquot was digested after X-ray fluorescence analysis[9]. Samples A0106 and C0107 were 17.15-mg and 17.36-mg powdered samples that were processed for sequential extraction of SOM using hexane, dichloromethane, methanol and water[57]. The residues with masses of 14.61 mg and 12.78 mg, respectively, were digested for the inorganic chemical and isotopic studies.

The six carbonaceous chondrite samples were investigated together with Ryugu samples. The Allende sample was taken from the Smithsonian bulk Allende reference powder that was homogenized from a 4-kg mass (USNM 3529, Split 20, Position 31). The Orgueil and Alais samples were powdered from approximately 50-mg crumbs provided by the National Museum of Natural History, France (n219 and n25, respectively). The Murchison, Tagish Lake and Tarda samples were powdered from 1,645-mg, 1,055-mg and 212-mg chips purchased from the Michael Farmer Meteorites, Meteorite Market and Meteorite.fr, respectively. The masses of individual sample aliquots digested for Lu–Hf isotopic analyses are listed in Extended Data Table 1. In addition, 12 mg of powder of Orgueil and Tarda (aliquots different from those analysed for Lu–Hf isotopes) were used for SOM extraction tests, where the amounts of various elements recovered by the four-step procedures were measured (Extended Data Table 3). The total yields of Lu and Hf were ≤1%, indicating an insignificant effect of the SOM extraction on the Lu–Hf isotope systematics of the Ryugu samples A0106 and C0107. By contrast, we found significant elution of alkali and alkaline-earth elements into water as well as methanol (Extended Data Fig. 5).

The sample digestions were conducted with a mixture of concentrated hydrofluoric and nitric acids (HF and HNO_3) in tightly capped teflon vials at 180 °C for at least 3 days until the colours of precipitates and solutions of the samples changed from black to white and from dark reddish-brown to pale yellow, respectively. The digested samples were converted to a soluble form by treatments with concentrated HNO_3–HCl (hydrochloric acid) and concentrated HNO_3–H_2O_2 (hydrogen peroxide solution) mixtures, and dissolved in 5 ml of 0.5 M HNO_3. No visible precipitates were observed in the sample solutions. Approximately 8% of the solutions were used for chemical analyses of ref. 9 and this study, whereas approximately 80% were processed through sequential column chemistry[58] for individual isotopic ratio measurements of multiple elements including Mg (ref. 59), iron (Fe; ref. 60), titanium (Ti), chromium (Cr; refs. 9,61), molybdenum (Mo; ref. 62), neodymium (Nd) and Sm (ref. 35). Before splitting the sample solutions, ultrasonic agitation was performed for about 1 h to prevent elemental fractionation even when invisible precipitates existed. In addition, other fractions of the solutions were analysed for calcium (Ca; ref. 63), copper (Cu) and zinc (Zn; ref. 64) isotopes after column chemistry. For this study, Hf for determination of its isotopic composition was purified from the Hf–zirconium (Zr) elution cut from DGA resin for the Ti column chemistry[9,61], whereas Lu was purified from the heavy REE elution cut from Ln resin for the Nd–Sm column chemistry[35]. The Hf–Zr elution was dried down, re-dissolved in 2.5 M HCl, and loaded onto a Teflon column packed with approximately 0.1 ml of Ln resin (100–150 μm). On the basis of the protocol in ref. 65, Zr was released from the column in 6 M HNO_3 + 0.06 M HF and subsequently Hf was collected in 2 M HF. The heavy REE elution was dried down, re-dissolved in 3.3 M HCl, and loaded onto an approximately 120-mm-long Teflon column packed with approximately 1 ml of Ln resin (20–50 μm). Following ref. 66, all REEs except Lu were eluted with 3.3 M HCl and then Lu was collected in 6 M HCl. This Lu process was repeated to further reduce the residual amount of ytterbium (Yb) that causes isobaric interference on ^{176}Lu.

The sample solutions for elemental abundance determination were weighed and divided into three solutions for the measurements of (1) major elements, (2) high-field-strength elements (HFSE) including Hf, and (3) other elements including REEs, followed by weighing of the three solutions. The major element solutions were doped with approximately 60 ng Rh of the internal standard and diluted with 0.5 M HNO_3. The HFSE solutions were spiked with a mixed ^{48}Ti–^{91}Zr–^{97}Mo–^{179}Hf–^{182}W tracer for isotope dilution and diluted with 0.5 M HNO_3–0.05 M HF. The REE solutions including Lu were doped with a mixed ^{113}In–^{203}Tl tracer for internal standardization and diluted with 0.5 M HNO_3. These diluted sample solutions were measured with a Thermo Fisher Scientific X-series 2 quadrupole-inductively coupled plasma mass spectrometer (Q-ICPMS) at the Institute of Science Tokyo (Extended Data Table 4 and Extended Data Fig. 5). The analytical method has been described in detail previously[9,67]. As for Hf abundances, the residual HFSE solutions from Q-ICPMS analysis were processed through a tandem column extraction of Hf. An approximately 0.05 ml AG1-X8 resin (200–400 mesh) column was placed on top of an approximately 0.1 ml Ln resin (100–150 μm) column. The samples were loaded onto the tandem columns and washed with 6 M HCl, in which most matrix elements and Hf pass through the AG1-X8 column, whereas Fe and U are retained by the column. After decoupling of the columns, Ti retained by the Ln resin column was eluted with 0.5 M HNO_3 + 1% H_2O_2, followed by Hf extraction in 2 M HF. The separated Hf fractions were analysed by multiple collector (MC)-ICPMS. These series of chemical processes for chemical and isotopic analyses of Ryugu samples are summarized in Extended Data Fig. 7.

MC-ICPMS

The Hf and Lu isotopic analyses were performed on a NEPTUNE plus MC-ICPMS (Thermo Fisher Scientific) attached to an Aridus II desolvating nebulizer (Cetac Technologies) at the University of Tokyo. The samples were introduced to the instrument with an uptake rate of approximately 150 μl min^{-1}. All instrumental mass bias effects were corrected using an exponential law. For Hf isotopic analyses, high-transmission Jet-sample and X-skimmer cones were utilized, resulting in the sensitivity of 1×10^{-11}–2×10^{-11} A per parts per billion (ppb) for total Hf. The separated Hf fractions for the determination of its isotopic composition (unspiked samples) were dissolved in 1.2 ml of 0.5 M HNO_3 with a trace amount (about 0.001 M) of HF, resulting in the total Hf signal intensities of 2×10^{-11}–4×10^{-11} A. The total Hf procedural blanks from sample digestion to final isotopic analysis were 2.6 ± 2.5 pg (2 s.d., n = 4), whose effects on the ^{176}Hf/^{177}Hf values of the Ryugu samples are less than approximately 50% of the reported errors. Data were acquired over about 100 cycles with an integration time of 4.0 s for the samples. Nine Faraday cups connected to amplifiers with 10^{11}-Ω resistors were set to monitor ^{172}Yb, ^{174}(Hf+Yb), ^{175}Lu, ^{176}(Hf+Yb+Lu), ^{177}Hf, ^{178}Hf, ^{179}Hf, ^{180}(Hf+W+Ta) and ^{182}W. We found that the interferences of Lu and tantalum (Ta) on Hf isotopes are negligible owing to efficient removal of these elements in the column chemistry. For the interference corrections of Yb and tungsten (W), we used the literature values of ^{176}Yb/^{172}Yb = 0.579397, ^{174}Yb/^{172}Yb = 1.45198 (ref. 68) and ^{180}W/^{182}W = 0.00452 (ref. 69), assuming that the mass bias factors of Yb and W are identical to that of Hf. The validity of this assumption was

confirmed by measuring 2-ppb JMC-Hf 475 standard solutions doped with Yb and W at the levels of more than one order of magnitude higher than the analysed samples. The Hf mass bias factor was calculated by normalizing to $^{179}Hf/^{177}Hf = 0.7325$. To ensure accurate comparison with literature values, sample $^{176}Hf/^{177}Hf$ values corrected for the isobaric interference and mass bias were further normalized to a reference value of $^{176}Hf/^{177}Hf = 0.282160$ for the means of the bracketing 2-ppb JMC-Hf 475 standard runs which averaged at 0.282150 ± 15 (2 s.d., $n = 41$) over the course of this study. Non-radiogenic Hf isotopic ratios corrected for the mass bias are reported in ε deviations from the standard:

$$\varepsilon^{i}\mathrm{Hf} = \left[\left(\frac{^{i}\mathrm{Hf}}{^{177}\mathrm{Hf}} \right)_{\mathrm{sample}} \Big/ \left(\frac{^{i}\mathrm{Hf}}{^{177}\mathrm{Hf}} \right)_{\mathrm{JMC-Hf475}} - 1 \right] \times 10^{4}. \quad (2)$$

The separated Hf fractions spiked with a ^{179}Hf tracer for the abundance determination were dissolved in 0.5 ml of 0.5 M HNO_3 with a trace amount of HF and analysed for $^{179}Hf/^{178}Hf$. The sample solutions were doped with a SPEX Yb standard solution to correct for instrumental mass bias by normalizing to $^{173}Yb/^{171}Yb = 1.12346$ (ref. 68). Data acquisition was performed in a static mode with an integration time of 2.0 s over about 80 cycles. Faraday cups with 10^{11}-Ω amplifiers were used to monitor ^{179}Hf, ^{171}Yb and ^{173}Yb, whereas that with a 10^{13}-Ω amplifier was used for ^{178}Hf. The ^{178}Hf signal intensities obtained during the sample analyses were approximately 2×10^{-13} A, whereas those of 5 procedural blanks from the column chemistry were $(1.9 \pm 1.0) \times 10^{-15}$ A. Uncertainties arising from the blank correction are included in the reported errors. The Hf abundances determined by MC-ICPMS for separated Hf solutions (Extended Data Table 1) were consistent within the uncertainty with less precise abundances obtained by Q-ICPMS for unseparated solutions (Extended Data Table 4). The $^{176}Lu/^{177}Hf$ values shown in Fig. 1 and Extended Data Table 1 were calculated from the former Hf abundances and the Lu abundances determined by Q-ICPMS[9] (Extended Data Table 4).

For the determination of Lu isotopic compositions of unspiked samples, we utilized a standard sample cone instead of the high-transmission Jet-sample cone. The typical sensitivity achieved with this cone set-up was approximately 2×10^{-11} A ppb^{-1} for total Lu. The separated Lu fractions of the samples were dissolved in 0.5 ml of 0.5 M HNO_3 and doped with NIST SRM 3163W standard for instrumental mass bias correction. The samples gave total Lu signal intensities of approximately 2×10^{-11} A, whereas the procedural blanks from the Ln resin column chemistry for Lu separation yielded approximately 2×10^{-15} A. Data were acquired using an integration time of 2.0 s over about 90 cycles. The collector array was set to monitor ^{172}Yb, ^{173}Yb, ^{175}Lu, ^{176}(Lu+Yb+Hf), ^{177}Hf, ^{179}Hf, ^{182}W, ^{184}W and ^{186}W. Faraday cups were used to collect all the isotopes except ^{177}Hf, for which a secondary electron multiplier was used. Amplifiers with 10^{13}-Ω resistors were assigned to the Faraday cups monitoring ^{173}Yb and ^{176}(Lu+Yb+Hf), whereas those with 10^{11}-Ω resistors were connected to the others. We found that the responses of the 10^{13}-Ω amplifier are not fast enough to follow signal intensity changes even after applying the conventional τ correction, as illustrated by the correlation between the measured Lu isotopic ratio and rate of signal intensity change. Following the protocol in ref. 70, the differential responses of the 10^{13}-Ω from 10^{11}-Ω amplifiers were calibrated using the correlation factors determined from $^{235}U/^{238}U$ measurements of a monazite standard using laser ablation-MC-ICPMS under artificially fluctuated signal intensities by switching the spot size. This empirical calibration improved the internal precisions by factors of about two. The mass bias factor was calculated by normalizing to $^{186}W/^{184}W = 0.92767$ (ref. 69). After the amplifier response calibration, the isobaric interferences by ^{176}Yb and ^{176}Hf on ^{176}Lu were estimated from ^{173}Yb and ^{177}Hf signals, respectively. For the interference correction, $^{176}Yb/^{173}Yb$ and $^{176}Hf/^{177}Hf$ were modified from the literature values to eliminate spurious isotopic anomalies for Yb- and Hf-doped Lu standard solutions. This is a practical way to account for the actual difference of the mass bias factors of Yb and Hf from that of W. To compensate the mass bias difference between Lu and W, one or two sample measurements were bracketed by six analyses of a SPEX Lu standard solution doped with NIST SRM 3163W standard. We found that the SPEX Lu standard has a lower $^{176}Lu/^{175}Lu$ by 0.22 ± 0.08‰ (2 s.d.) relative to NIST SRM 3130a Lu standard solution used in previous studies[31,66]. For comparison with literature values, sample $^{176}Lu/^{175}Lu$ values are reported in δ values defined as:

$$\delta^{176}\mathrm{Lu} = \left[\left(\frac{^{176}\mathrm{Lu}}{^{175}\mathrm{Lu}} \right)_{\mathrm{sample}} \Big/ \left(\frac{^{176}\mathrm{Lu}}{^{175}\mathrm{Lu}} \right)_{\mathrm{SPEX}} - 1 \right] \times 10^{3} - 0.22. \quad (3)$$

The total Lu yields of the chemical separation procedure were 70–80% for Ryugu samples, except for C0108 with a 40% yield. These procedural yields were lower than in previous studies[30,31,66], probably owing to incomplete Lu recovery during the REE separation using Ln resin. Such incomplete recovery could potentially be accompanied by $^{176}Lu/^{175}Lu$ fractionation. To quantify the degree of Lu isotope fractionation induced by the Ln resin chromatography, the SPEX Lu standard solution was passed through the resin, and successive elution fractions were analysed for Lu isotope composition relative to the unprocessed standard. The results are presented in Extended Data Fig. 8, showing that even when the Lu recovery is as low as 10%, $^{176}Lu/^{175}Lu$ is fractionated only by about 0.1‰, which is smaller than analytical uncertainties of about 0.2‰ for Ryugu samples.

Correction for the nucleosynthetic effect on Hf isotopes

Non-radiogenic Hf isotopic compositions of extraterrestrial samples are variable owing to either the heterogeneous distribution of an s-process component[32,33,71,72] or the capture of secondary cosmogenic neutrons[36,73]. As nucleosynthetic and neutron-capture effects produce near-orthogonal trends in $\varepsilon^{180}Hf$–$\varepsilon^{178}Hf$ space (Fig. 2), we can use those measurements to differentiate the two effects[73,74]. The positively correlated $\varepsilon^{180}Hf$–$\varepsilon^{178}Hf$ variations in our samples can be attributed solely to nucleosynthetic effects. The range of allowable cosmogenic $\varepsilon^{178}Hf$ variations can be estimated by:

$$\varepsilon^{178}\mathrm{Hf}_{\mathrm{corr}} = \frac{s_{\mathrm{ns},180/178}\varepsilon^{178}\mathrm{Hf} - \varepsilon^{180}\mathrm{Hf}}{s_{\mathrm{ns},180/178} - s_{\mathrm{nc},180/178}}, \quad (4)$$

where the subscript 'corr' refers to corrected for nucleosynthetic effects, $s_{\mathrm{ns},180/178} = 1.215$ (ref. 34) and $s_{\mathrm{nc},180/178} = -1.58$ (ref. 36) are the slopes between $\varepsilon^{180}Hf$ and $\varepsilon^{178}Hf$ variations produced by nucleosynthetic and neutron-capture effects, respectively. The obtained $\varepsilon^{178}Hf_{\mathrm{corr}}$ values (Extended Data Table 1) show no resolvable variations within the limits of about 0.2 ε uncertainty. Hence, although mass-bias-corrected $^{176}Hf/^{177}Hf$ could be affected by both nucleosynthetic heterogeneity and neutron captures, only the former effect was corrected for our samples by:

$$\left(\frac{^{176}\mathrm{Hf}}{^{177}\mathrm{Hf}} \right)_{\mathrm{corr}} = \frac{^{176}\mathrm{Hf}}{^{177}\mathrm{Hf}} \left(1 - \frac{s_{\mathrm{ns},176/180}\varepsilon^{180}\mathrm{Hf}}{10^{4}} \right), \quad (5)$$

where $s_{\mathrm{ns},176/180} = 2.57$ (ref. 34) is the slope between $\varepsilon^{180}Hf$ and $\varepsilon^{176}Hf$ variations produced by the nucleosynthetic effect.

Constraints on cosmogenic neutron fluences and ^{176}Hf excess

Samarium isotopic analysis of the same digestions of our samples revealed deficits in ^{149}Sm accompanied by excesses in ^{150}Sm as expected for cosmogenic neutron capture on ^{149}Sm (ref. 35). Assuming that the Sm isotopic shifts reflect the capture exclusively of thermal neutrons, thermal neutron fluences of Ryugu samples were estimated to be from $(0.22 \pm 2.40) \times 10^{15}$ n cm^{-2} to $(3.43 \pm 0.84) \times 10^{15}$ n cm^{-2}. This

assumption is supported by no resolvable variation in $\varepsilon^{178}Hf_{corr}$ because it is affected predominantly by epithermal neutron captures[36,74]. To constrain the thermal and epithermal neutron fluences more rigorously, we modelled cosmogenic shifts in $^{178}Hf/^{177}Hf$ and $^{149}Sm/^{152}Sm$ using the approach of ref. 73, where the effect of spurious mass bias correction is included. Following ref. 35, the Sm mass bias was normalized to $^{147}Sm/^{152}Sm = 0.56081$. Taking into account all neutron-capture reactions relevant for the isotopes, the net changes in the isotopic abundances (N) were calculated as a function of the thermal (Φ) and epithermal (Θ) neutron fluences[75]:

$$dN_i = \sum N_{i-1}(\sigma_{i-1}^{th}\Phi + I_{i-1}\Theta) - N_i(\sigma_i^{th}\Phi + I_i\Theta), \quad (6)$$

where subscript i refers to a particular isotope, σ^{th} and I are the thermal neutron-capture cross-section and the resonance integral, respectively. The σ^{th} and I values were taken from ref. 76. The modelling results (Extended Data Fig. 1) show that the $\varepsilon^{178}Hf_{corr}$ values of our samples constrain epithermal neutron fluences to less than 8×10^{15} n cm^{-2}, and also that under such conditions $^{149}Sm/^{152}Sm$ shifts arising from epithermal neutron captures are smaller than the analytical uncertainty, validating the preceding estimates of thermal neutron fluence[35].

We further assessed the limits of ^{176}Hf excess in our samples that can be produced by reactions with cosmogenic neutrons. Two neutron-induced reactions potentially produce ^{176m}Lu that shortly decays to ^{176}Hf (ref. 16). One is the neutron capture on ^{175}Lu and the other is the neutron inelastic scattering on ^{176}Lu. In addition, ^{176}Hf is transformed to ^{177}Hf by neutron captures. Whereas the neutron-capture reactions are caused by both thermal and epithermal neutrons, the inelastic scattering is induced by only epithermal neutrons with energy higher than 123 keV. Hence, the net change in ^{176}Hf abundance is given by:

$$\begin{aligned} dN_{176Hf} = {} & N_{175Lu}\left(\sigma_{175Lu}^{th} f_{176mLu}^{th}\Phi + I_{175Lu} f_{176mLu}^{ep}\Theta\right) \\ & + N_{176Lu}\sigma_{176Lu}^{in}\Theta - N_{176Hf}(\sigma_{176Hf}^{th}\Phi + I_{176Hf}\Theta), \end{aligned} \quad (7)$$

where f_{176mLu}^{th} and f_{176mLu}^{ep} are the fractions of the short-lived isomer in all ^{176}Lu produced by thermal and epithermal neutron captures, respectively, and σ_{176Lu}^{in} is the inelastic scattering cross-section of ^{176}Lu. The f_{176mLu} and σ_{176Lu}^{in} values were taken from ref. 76 and the EXFOR database[77], respectively. Then, mass-bias-corrected $^{176}Hf/^{177}Hf$ values were calculated for the range of allowable neutron fluences on our samples ($\Theta \le 8 \times 10^{15}$ n cm^{-2} and $\Phi \le 4 \times 10^{15}$ n cm^{-2}). The results (Extended Data Fig. 2) show that ^{176}Hf excess due to neutron-induced reactions can be no more than about 1 ε, which is significantly smaller than the observed shifts of the Ryugu samples from the reference isochron.

The probable range of the original Lu abundance

In Ryugu fragments and CI chondrites, REEs including Lu are concentrated in accessory apatite[7,8,24,25]. Heterogeneous distribution of apatite leads to REE abundance variation between different samples especially when the analysed sample mass is small (the nugget effect). On the basis of REE-P co-enrichments in our Ryugu samples, we consider that their variable current Lu abundances resulted primarily from the apatite nugget effect and, to a lesser extent, from the secondary Lu loss. The dispersion of elemental abundance due to the nugget effect can be related to the sample mass m through the following relation[43]:

$$\sigma_C = \frac{|C_{nugget} - C_{matrix}|\rho_{nugget}\rho_{matrix}}{\left[f\rho_{nugget} + (1-f)\rho_{matrix}\right]^{3/2}}\sqrt{\frac{f(1-f)\pi d^3}{6m}}, \quad (8)$$

where f and d are the volume fraction and diameter of the nugget, ρ_{nugget} and ρ_{matrix} are the densities of the nugget and matrix, and C_{nugget} and C_{matrix} are the elemental mass fraction of the nugget and matrix, respectively. The bulk elemental mass fraction is given by:

$$\bar{C} = \frac{f\rho_{nugget}C_{nugget} + (1-f)\rho_{matrix}C_{matrix}}{f\rho_{nugget} + (1-f)\rho_{matrix}}. \quad (9)$$

Ryugu apatite grains are up to 80 μm in length (d) and enriched in REEs approximately 150 times relative to the CI chondrite mean, corresponding to $C_{nugget}^{Lu} \approx 3.7$ μg g^{-1} (refs. 8,9,24). The original Lu mass fraction and apatite volume fraction of the bulk Ryugu sample are unknown but expected to be similar to those of mean CI chondrites. Although measured elemental abundances of CI chondrites could be also dispersed and biased owing to the nugget effect, such bias can be mitigated either by increasing the sample size or by taking the weighted mean of a number of measurements. Indeed, Lu abundances measured for large-sized (approximately 1 g) CI chondrite samples[78,79] are identical within 8% to the weighted mean value of 0.0249 μg g^{-1} (ref. 80). Given that hydroxyapatite is the major host of P, the mean CI chondrite P abundance of 978 μg g^{-1} (ref. 80) indicates that the mass fraction of apatite is 0.528 wt%. Correcting for the 10% H_2O depletion in Ryugu samples relative to mean CI chondrites[9] and using the densities of hydroxyapatite ($\rho_{nugget} = 3.16$ g cm^{-3}) and mean CI chondrite grains ($\rho_{matrix} = 2.42$ g cm^{-3}: ref. 81), we derive an f value of 0.45%. Furthermore, the C_{matrix}^{Lu} value is set at 0.011 μg g^{-1} to be consistent with the mean CI chondrite Lu abundance ($\bar{C}^{Lu} = 0.0277$ μg g^{-1}, a modified value of ref. 80 for the H_2O depletion). The matrix Lu would be contained in or adsorbed on phyllosilicates and dolomite[7,82]. It is noted that Lu abundance variation arising from uneven distribution of these phases would be minor because of their lower Lu concentrations relative to apatite. Substituting the above f, d, C and ρ values into equation (8), the original Lu abundance in the Ryugu samples A0106 (17.15 mg), A0106-A0107 (23.88 mg), C0107 (17.36 mg) and C0108 (22.24 mg) can be estimated to be in the ranges of 0.0234–0.0319 μg g^{-1}, 0.0243–0.0310 μg g^{-1}, 0.0231–0.0322 μg g^{-1} and 0.0242–0.0311 μg g^{-1} at 95% confidence, respectively.

More conservative and robust estimates can be made by considering the presence of approximately 500-μm clasts with significantly high abundances of Ca-phosphate, most likely apatite (8.25 wt%), in CI chondrites[25]. When such an apatite-rich clast is regarded as a nugget, the parameters in equation (8) change as follows: $f = 6.3\%$, $\rho_{nugget} = 2.47$ g cm^{-3}, $C_{nugget}^{Lu} = 0.34$ μg g^{-1} and $C_{matrix}^{Lu} = 0.0064$ μg g^{-1}. In addition, because coarse clasts should be disaggregated during the sample powdering process, masses of not acid-digested but powdered samples are assigned to m. Accordingly, the 95% confidence intervals of A0106 (17.15 mg), A0106-A0107 (28.89 mg), C0107 (17.36 mg) and C0108 (33.34 mg) become 0.0120–0.0434 μg g^{-1}, 0.0156–0.0398 μg g^{-1}, 0.0121–0.0433 μg g^{-1} and 0.0164–0.0389 μg g^{-1}, respectively. By comparing these original Lu abundance ranges with the present Lu abundances in the samples, the upper limits on the proportion of lost Lu can be estimated to be 17%, 14%, 27% and 20% for A0106, A0106-A0107, C0107 and C0108, respectively (Fig. 3 and Extended Data Fig. 4).

Thermodynamic modelling

We conducted thermodynamic modelling of the aqueous alteration on the Ryugu parent body, following the approach of ref. 83. Chemical equilibria were calculated for a closed 14-element (H, C, O, S, Cl, Si, Mg, Fe, Ca, Al, Na, K, Mn, P) solid–liquid system. The initial rock was represented by H_2O–CO_2-free mean composition of CI chondrites (after ref. 80). This rock was mixed with water in different proportions. Reflecting the presence of a CO_2-bearing fluid inclusion in a Ryugu pyrrhotite[8], the water is assumed to contain CO_2 at 3 mol%. Chemical equilibrium calculations were performed using the EQ3/6 software package[84]. The B-dot activity model was used in the calculations[85,86]. The temperature-dependent activity coefficient for aqueous CO_2 was derived from the empirical relationship established by ref. 87.

The thermodynamic database for the calculations was generated by SUPCRT92 software[88] with thermodynamic data for mineral and

aqueous species and complexes[83,89–95]. Solid solutions are assumed as ideal mixing in the modelling. However, Fe–Mg substitution was not considered for saponite because of the Mg-rich composition of Ryugu saponite[7,8]. Calcium-phosphate and Fe-sulfide are assumed to be hydroxyapatite and pyrrhotite, respectively, as observed in Ryugu samples[8–10]. The precipitation of some minerals (for example, biotite, feldspar, chlorite and pyroxene) whose formation is kinetically limited at low temperatures, was inhibited. In this case, thermodynamically metastable minerals (for example, smectite group minerals) partially compose the alteration minerals[96]. In addition, Al hydroxides (for example, gibbsite and diaspore) frequently occur even at low temperatures in terrestrial environments and are expected to appear even in the modelling results. However, they are generally absent or occur as minor phases in carbonaceous chondrites[97]. Thus, these minerals are not considered in our modelling.

During the fluid–rock reactions, the consumption of water through formation of hydrous and oxidized minerals substantially condenses the dissolved species in solutions under conditions of a low initial water/rock mass ratio (W/R), which elevates ionic strength beyond the appropriate values of modelling (2–3 molal). Therefore, the initial W/R was changed from 0.2 to 10 in the modelling. The equilibrium temperature and pressure were set to be 40 °C (ref. 9) and 1 bar, respectively. The fugacity of H_2 in the equilibrium state was set to an approximate value of quartz–fayalite–magnetite buffer at 40 °C ($\log fH_2 = -1.5$). For simplicity, organic synthesis derived from CO_2 reduction was not considered.

The assemblage and abundances of minerals change with W/R (Extended Data Fig. 6a). Serpentine and saponite are predominant as phyllosilicates at W/R of <2, whereas kaolinite and Fe-beidellite also exist as the minor phyllosilicates in some cases. Rhodochrosite numerically appears at all W/Rs but in natural systems it is probably incorporated into other main carbonate minerals as solid solution or impurity. Pyrrhotite is present at all W/R. As W/R decreases, the dominant carbonate minerals change from magnesite and siderite, to dolomite, to calcite. Hydroxyapatite appears at W/R values <0.8 as well as about 2, and its abundance is highest at low W/R values where calcite exists. The major lithology of Ryugu samples, which is characterized by the predominance of dolomite over calcite and magnesite[7,8,10], matches the modelled mineral assemblage at W/R values of 0.3 to 0.5, which is consistent with the estimate from O isotope systematics of CI chondrites[98,99]. We further calculated the mass fraction of water existing as structural OH of hydrous minerals and aqueous fluid in the equilibrium system by accounting for fluid consumption through formation of the hydrous minerals and of oxide minerals associated with H_2 degassing (Extended Data Fig. 6b). The total water content will be 20 wt% to 30 wt% at W/R values of 0.3 to 0.5 for Ryugu and CI chondrites. By contrast, the mineralogy and O isotope systematics of non-CI chondrites suggest early aqueous alteration at lower W/R values[98–100], where all initial fluid would have been consumed by formation of hydrous and oxide minerals. It follows that late fluid generation in the parent bodies would require the decomposition of the hydrous minerals.

Chemical consequences and possible causes of apatite dissolution

The mineralogical observations[10,24] indicate that Ryugu apatite formed during early aqueous alteration together with carbonate and magnetite, and it was partially dissolved by fluids during a later alteration episode. Apatite would incorporate the majority of the bulk REE budget but little Hf into its structure during crystallization. Subsequent partial dissolution of apatite released REEs to the co-existing fluids. Although the released REEs could be re-partitioned into the residual apatite under equilibrium conditions, such re-partitioning was probably inhibited owing to freezing of REE diffusion in apatite at <500 °C (ref. 101). Moreover, when the fluids were alkaline (about pH 10) alkali–carbonate solutions as inferred for Ryugu samples[8], they can dissolve significant amounts (hundreds of micrograms per gram) of REEs, especially heavy REEs, as hydroxyl-carbonate complexes[102]. Although late apatite dissolution could release radiogenic Hf, it is extremely insoluble in weakly to moderately alkaline fluids[103]. Consequently, escape of the fluids that dissolved apatite probably caused preferential loss of Lu over Hf from the Ryugu samples, leading to the observed shifts from the reference isochron. Such fluid escape would be accompanied by loss of Sm and Nd, which potentially disturbed the ^{147}Sm–^{143}Nd decay system. This may account for the observed offset of one Ryugu sample A0106-A0107 from a reference ^{147}Sm–^{143}Nd isochron for 4.57 Gyr (ref. 35). It is noted, however, that because Ryugu apatite shows only weakly fractionated chondrite-normalized REE patterns[7,8,24], fractionation of Sm/Nd owing to the fluid escape should be limited compared with that of Lu/Hf, rendering the Sm–Nd system less susceptible to the disturbance than the Lu–Hf system.

The ultimate cause of partial dissolution of once-formed apatite is unclear, but it probably involves changes in alteration conditions that control the stability of apatite. Our thermodynamic modelling (Extended Data Fig. 6) indicates that more abundant apatite is present at W/R values of <0.3 where the major carbonate phase is calcite instead of dolomite. Besides, the C, O and Mg isotopic signatures of Ryugu carbonates[104–106] indicate that calcite precipitated during the earliest stage of aqueous alteration, whereas dolomite formed under a more CO_2-rich environment when the system was approaching equilibrium. In addition, Ryugu apatite grains are often surrounded by dolomite, indicating earlier crystallization of the former[107]. On the basis of these results, it can be inferred that apatite was formed together with calcite during the earliest stage of early aqueous alteration, followed by its partial dissolution and replacement of calcite by dolomite when the system was approaching equilibrium. Furthermore, because apatite becomes less stable at lower temperatures[108], it could be partially dissolved upon cooling during the retrograde stage. In the case of apatite dissolution during the middle and/or late stages of the early aqueous alteration that ended within a few million years after the parent-body accretion[7,9,11], there should be a ≥1-Gyr gap from the apatite dissolution to the escape of the fluids for Lu removal. Alternatively, the apatite dissolution and fluid escape might be near-simultaneous if late-generated fluids could be reacted with pre-altered lithology under conditions where apatite is relatively unstable.

In light of the mineralogical and chemical similarities between Ryugu samples and CI chondrites, partial dissolution of apatite would be expected to have occurred in CI chondrites as well. Nevertheless, all but one CI chondrite data point plot on the 4,565-Myr reference Lu–Hf isochron (Fig. 1); the offset of one Orgueil data point was interpreted to reflect inaccuracy in isotope dilution $^{176}Lu/^{177}Hf$ analysis arising from incomplete equilibration between the sample and isotopic tracer[18]. The lack of apparent ^{176}Hf excesses in CI chondrites may reflect either that impact events on the parent body were not intense enough to enable fluid migration or that the events were intense enough but too early to produce detectable apparent ^{176}Hf excesses. Even in the latter case, no more than 20% Lu loss can be accommodated by the REE abundance match within uncertainty between mean CI chondrites and the solar photosphere[80].

Data availability

The whole Ryugu Sample Database is available from the Hayabusa2 Science Data Archives (DARTS; https://www.darts.isas.jaxa.jp/curation/hayabusa2/). The data generated in this study are provided in the Extended Data tables and are publicly available on Zenodo at https://doi.org/10.5281/zenodo.16462056 (ref. 109). Source data are provided with this paper.

56. Morota, T. et al. Sample collection from asteroid (162173) Ryugu by Hayabusa2: implications for surface evolution. *Science* **368**, 654–659 (2020).
57. Naraoka, H. et al. Soluble organic molecules in samples of the carbonaceous asteroid (162173) Ryugu. *Science* **379**, eabn9033 (2023).

58. Gautam, I., Yokoyama, T., Horan, M. F. & Carlson, R. W. Five-stage multielement separation procedure: a unique and essential tool for the multi-isotopic analyses of precious (<30 mg) extraterrestrial materials. *Geochem. J.* **59**, 64–83 (2025).
59. Bizzarro, M. et al. The magnesium isotope composition of samples returned from asteroid Ryugu. *Astrophys. J. Lett.* **958**, L25 (2023).
60. Hopp, T. et al. Ryugu's nucleosynthetic heritage from the outskirts of the Solar System. *Sci. Adv.* **8**, eadd8141 (2022).
61. Yokoyama, T. et al. Water circulation in Ryugu asteroid affected the distribution of nucleosynthetic isotope anomalies in returned sample. *Sci. Adv.* **9**, eadi7048 (2023).
62. Nakanishi, N. et al. Nucleosynthetic s-process depletion in Mo from Ryugu samples returned by Hayabusa2. *Geochem. Persp. Lett.* **28**, 31–36 (2023).
63. Moynier, F. et al. The Solar System calcium isotopic composition inferred from Ryugu samples. *Geochem. Persp. Lett.* **24**, 1–6 (2022).
64. Paquet, M. et al. Contribution of Ryugu-like material to Earth's volatile inventory by Cu and Zn isotopic analysis. *Nat. Astron.* **7**, 182–189 (2023).
65. Münker, C., Weyer, S., Scherer, E. & Mezger, K. Separation of high field strength elements (Nb, Ta, Zr, Hf) and Lu from rock samples for MC-ICPMS measurements. *Geochem. Geophys. Geosyst.* https://doi.org/10.1029/2001GC000183 (2001).
66. Wimpenny, J. B., Amelin, Y. & Yin, Q.-Z. Precise determination of the lutetium isotopic composition in rocks and minerals using multicollector ICPMS. *Anal. Chem.* **85**, 11258–11264 (2013).
67. Yokoyama, T., Nagai, Y., Hinohara, Y. & Mori, T. Investigating the influence of non-spectral matrix effects in the determination of twenty-two trace elements in rock samples by ICP-QMS. *Geostand. Geoanal. Res.* **41**, 221–242 (2016).
68. Thirlwall, M. F. & Anczkiewicz, R. Multidynamic isotope ratio analysis using MC–ICP–MS and the causes of secular drift in Hf, Nd and Pb isotope ratios. *Int. J. Mass Spectrom.* **235**, 59–81 (2004).
69. Völkening, J., Köppe, M. & Heumann, K. G. Tungsten isotope ratio determinations by negative thermal ionization mass spectrometry. *Int. J. Mass. Spectrom. Ion Proc.* **107**, 361–368 (1991).
70. Iizuka, T., Eggins, S. M., McCulloch, M. T., Kinsley, L. P. J. & Morimer, G. E. Precise and accurate determination of $^{147}Sm/^{144}Nd$ and $^{143}Nd/^{144}Nd$ in monazite using laser ablation-MC-ICPMS. *Chem. Geol.* **282**, 45–57 (2011).
71. Akram, W., Schönbächler, M., Sprung, P. & Vogel, N. Zirconium–hafnium isotope evidence from meteorites for the decoupled synthesis of light and heavy neutron-rich nuclei. *Astrophys. J.* **777**, 169 (2013).
72. Elfers, B.-M. et al. Variable distribution of s-process Hf and W isotope carriers in chondritic meteorites—evidence from ^{174}Hf and ^{180}W. *Geochim. Cosmochim. Acta* **239**, 346–362 (2018).
73. Sprung, P., Scherer, E. E., Upadhyay, D., Leya, I. & Mezger, K. Non-nucleosynthetic heterogeneity in non-radiogenic stable Hf isotopes: Implications for early Solar System chronology. *Earth Planet. Sci. Lett.* **295**, 1–11 (2010).
74. Chen, X. et al. Methodologies for ^{176}Lu–^{176}Hf analysis of zircon grains from the Moon and beyond. *ACS Earth Space Chem.* **8**, 36–53 (2024).
75. Nyquist, L. E. et al. ^{146}Sm–^{142}Nd formation interval for the lunar mantle. *Geochim. Cosmochim. Acta* **59**, 2817–2837 (1995).
76. Mughabghab, S. F. *Atlas of Neutron Resonances* Vol. 2 (Elsevier, 2018).
77. Otuka, N. et al. Towards a more complete and accurate experimental nuclear reaction data library (EXFOR): International collaboration between Nuclear Reaction Data Centres (NRDC). *Nucl. Data Sheets* **120**, 272–276 (2014).
78. Barrat, J. A. et al. Geochemistry of CI chondrites: major and trace elements, and Cu and Zn isotopes. *Geochim. Cosmochim. Acta* **83**, 79–92 (2012).
79. Beer, H., Walter, G., Macklin, R. L. & Patchett, P. J. Neutron capture cross sections and solar abundances of $^{160,161}Dy$, $^{170,171}Yb$, $^{175,176}Lu$, and $^{176,177}Hf$ for the s-process analysis of the radionuclide ^{176}Lu. *Phy. Rev. C* **30**, 464–478 (1984).
80. Lodders, K. Relative atomic solar system abundances, mass fractions, and atomic masses of the elements and their isotopes, composition of the solar photosphere, and compositions of the major chondritic meteorite groups. *Space Sci. Rev.* **217**, 44 (2021).
81. Macke, R. J., Consolmagno, G. J. & Britt, D. T. Density, porosity, and magnetic susceptibility of carbonaceous chondrites. *Meteorit. Planet. Sci.* **46**, 1842–1862 (2011).
82. Tack, P. et al. Rare earth element identification and quantification in millimetre-sized Ryugu rock fragments from the Hayabusa2 space mission. *Earth Planets Space* **74**, 146 (2022).
83. Shibuya, T. et al. Aqueous alteration in icy planetesimals: the effect of outward transport of gaseous hydrogen. *Geochim. Cosmochim. Acta* **374**, 264–283 (2024).
84. Wolery, T. W. & Larek, R. L. *Software User's Manual EQ3/6, Version 8.0* (Sandia National Laboratories, 2003).
85. Helgeson, H. C. Thermodynamics of hydrothermal systems at elevated temperatures and pressures. *Am. J. Sci.* **267**, 729–804 (1969).
86. Helgeson, H. C. & Kirkham, D. H. Theoretical prediction of the thermodynamic behavior of aqueous electrolytes at high pressures and temperatures; II, Debye–Hückel parameters for activity coefficients and relative partial molal properties. *Am. J. Sci.* **274**, 1199–1261 (1974).
87. Drummond, S. E. *Boiling and Mixing of Hydrothermal Fluids: Chemical Effects on Mineral Precipitation*. PhD thesis, Pennsylvania State Univ. (1981).
88. Johnson, J. W., Oelkers, E. H. & Helgeson, H. C. SUPCRT92: a software package for calculating the standard molal thermodynamic properties of minerals, gases, aqueous species, and reactions from 1 to 5000 bar and 0 to 1000 °C. *Comput. Geosci.* **18**, 899–947 (1992).
89. Helgeson, H. C., Delany, J. M., Nesbitt, H. W. & Bird, D. K. Summary and critique of the thermodynamic properties of rock-forming minerals. *Am. J. Sci.* **278-A**, 1–229 (1978).
90. Shock, E. L. & Helgeson, H. C. Calculation of the thermodynamic and transport properties of aqueous species at high pressures and temperatures: correlation algorithms for ionic species and equation of state predictions to 5 kb and 1000 °C. *Geochim. Cosmochim. Acta* **52**, 2009–2036 (1988).
91. Shock, E. L., Helgeson, H. C. & Sverjensky, D. A. Calculation of the thermodynamic and transport properties of aqueous species at high pressures and temperatures: standard partial molal properties of inorganic neutral species. *Geochim. Cosmochim. Acta* **53**, 2157–2183 (1989).
92. Shock, E. L. & Koretsky, C. M. Metal–organic complexes in geochemical processes: estimation of standard partial molal thermodynamic properties of aqueous complexes between metal cations and monovalent organic acid ligands at high pressures and temperatures. *Geochim. Cosmochim. Acta* **59**, 1497–1532 (1995).
93. Shock, E. L., Sassani, D. C., Willis, M. & Sverjensky, D. A. Inorganic species in geologic fluids: correlations among standard molal thermodynamic properties of aqueous ions and hydroxide complexes. *Geochim. Cosmochim. Acta* **61**, 907–950 (1997).
94. Sverjensky, D. A., Shock, E. L. & Helgeson, H. C. Prediction of the thermodynamic properties of aqueous metal complexes to 1000 °C and 5 kb. *Geochim. Cosmochim. Acta* **61**, 1359–1412 (1997).
95. McCollom, T. M. & Bach, W. Thermodynamic constraints on hydrogen generation during serpentinization of ultramafic rocks. *Geochim. Cosmochim. Acta* **73**, 856–875 (2009).
96. Zolotov, M. Y. Aqueous fluid composition in CI chondritic materials: Chemical equilibrium assessments in closed systems. *Icarus* **220**, 713–729 (2012).
97. Brearly, A. J. in *Meteorites and the Early Solar System II* (eds Lauretta, D. S. & McSween, H. Y.) 587–624 (Univ. Arizona Press, 2006).
98. Zolensky, M. E. et al. CM chondrites exhibit the complete petrologic range from type 2 to 1. *Geochim. Cosmochim. Acta* **61**, 5099–5115 (1997).
99. Clayton, R. N. & Mayeda, T. K. Oxygen isotope studies of carbonaceous chondrites. *Geochim. Cosmochim. Acta* **63**, 2089–2104 (1999).
100. Zolensky, M., Barrett, R. & Browning, L. Mineralogy and composition of matrix and chondrule rims in carbonaceous chondrites. *Geochim. Cosmochim. Acta* **57**, 3123–3148 (1993).
101. Cherniak, D. J. Rare earth element diffusion in apatite. *Geochim. Cosmochim. Acta* **64**, 3871–3885 (2000).
102. Louvel, M., Etschmann, B., Guan, Q., Testemale, D. & Brugger, J. Carbonate complexation enhances hydrothermal transport of rare earth elements in alkaline fluids. *Nat. Commun.* **13**, 1456 (2022).
103. Rai, D., Xia, Y., Hess, N. J., Strachan, D. M. & McGrail, B. P. Hydroxo and chloro complexes/ion interaction of Hf^{4+} and the solubility product of HfO_2(am). *J. Solution Chem.* **30**, 949–967 (2001).
104. Fujiya, W. et al. Carbonate record of temporal change in oxygen fugacity and gaseous species in asteroid Ryugu. *Nat. Geosci.* **16**, 675–682 (2023).
105. Kita, N. T. et al. Disequilibrium oxygen isotope distribution among aqueously altered minerals in Ryugu asteroid returned samples. *Meteorit. Planet. Sci.* **59**, 2097–2116 (2024).
106. Yoshimura, T. et al. Breunnerite grain and magnesium isotope chemistry reveal cation partitioning during aqueous alteration of asteroid Ryugu. *Nat. Commun.* **15**, 6809 (2024).
107. Tsuchiyama, A. et al. Three-dimensional textures of Ryugu samples and their implications for the evolution of aqueous alteration in the Ryugu parent body. *Geochim. Cosmochim. Acta* **375**, 146–172 (2024).
108. Postberg, F. et al. Detection of phosphates originating from Enceladus's ocean. *Nature* **618**, 489–493 (2023).
109. Iizuka, T. & Hayabusa2-initial-analysis chemistry team Repository: Late fluid flow in a primitive asteroid revealed by Lu–Hf isotopes in Ryugu [Dataset]. *Zenodo* https://doi.org/10.5281/zenodo.16462056 (2025).
110. Lodders, K. Solar System abundances and condensation temperatures of the elements. *Astrophys. J.* **591**, 1220–1247 (2003).

Acknowledgements We thank the National Museum of Natural History, France and the Smithsonian National Museum of Natural History for meteorite samples. We are grateful to T. Kogure, K. Hamano, H. Sakuma, Y. Takano, T. Yoshimura, and K. Hirose for discussions. Hayabusa2 was developed and built under the leadership of the Japan Aerospace Exploration Agency (JAXA), with contributions from the German Aerospace Center (DLR) and in collaboration with NASA and other universities, institutes and companies in Japan. The curation system was developed by JAXA in collaboration with companies in Japan. This work was supported by Japan Society for the Promotion of Science KAKENHI grants (21KK0057, 22H00170).

Author contributions T.I., T. Yokoyama and H. Yurimoto designed this study. T. Yokoyama, I.G. and T.I. separated Hf and Lu from the matrix. M.K.H., K.T.M.I. and Y.H. supported the separation. T. Yokoyama and H.N. conducted the SOM extraction tests. T.I. and T. Yokoyama were responsible for data acquisition and interpretation. T. Shibuya carried out thermodynamic modelling. T.I. wrote the initial draft of the paper, with contributions from T.H., T. Shibuya and T. Yokoyama. The draft was edited by N.D., A.B., Y. Amelin, Q.-Z.Y., M.W., T.H., T. Yokoyama, K.T.M.I., Y.H., A.Y., H.N., S. Tachiband and H. Yurimoto. The paper was reviewed and approved by T.I., T. Shibuya, T.H., T. Yokoyama, I.G., M.K.H., K.T.M.I., Y.H., A.Y., Y. Abe, J.A., C.M.O'D.A, S.A., Y. Amelin, K.-i.B., M.B., A.B., R.W.C., M.C., B.-G.C., N.D., A.M.D., T.D.R., W.F., R.F., H. Hidaka, H. Homma, G.R.H., T.R.I., A.I., S.I., N.K., N.T.K., K.K., T.K., S.K., A.N.K., M.-C.L., Y.M., K.M., F.M., K.N., I.N., A. Nguyen, L.N., A.P., C.P., L.P., L.Q., S.R., N.S., M.S., L.T., H.T., K.T., Y. Terada, T.U., S.W., M.W., R.J.W., K. Yamashita, Q.-Z.Y., S.Y., H. Yui, A.-C.Z., T. Nakamura, H.N., T. Noguchi, R.O., K.S., H. Yabuta, M.A., A.M., A. Nakato, M.N., T.O., T. Yada, K. Yogata, S.N., T. Saiki, S. Tanaka, F.T., Y. Tsuda, S.-i.W., M.Y., S. Tachiband and H. Yurimoto.

Competing interests The authors declare no competing interests.

Additional information

Supplementary information The online version contains supplementary material available at https://doi.org/10.1038/s41586-025-09483-0.

Correspondence and requests for materials should be addressed to Tsuyoshi Iizuka.

Peer review information *Nature* thanks Vinciane Debaille and Erik Scherer for their contribution to the peer review of this work. Peer reviewer reports are available.

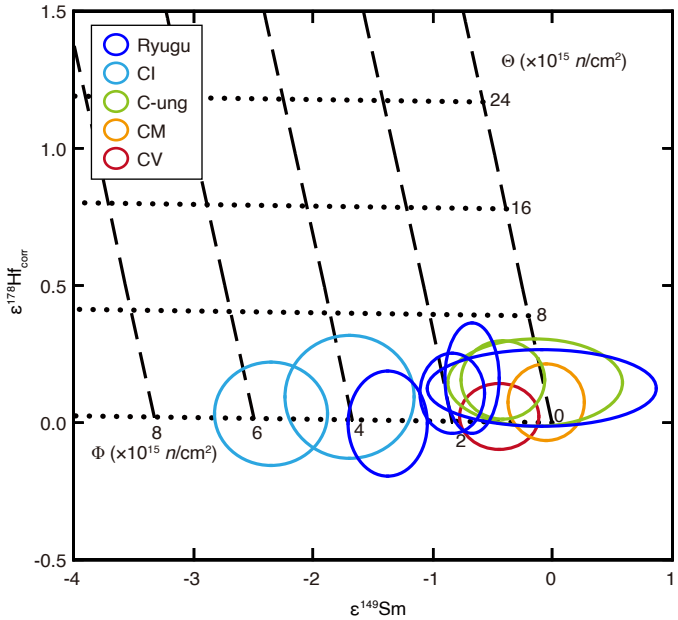

Extended Data Fig. 1 | Plot of $\varepsilon^{178}Hf_{corr}$ versus $\varepsilon^{149}Sm$ for Ryugu and carbonaceous chondrite samples. The $\varepsilon^{178}Hf_{corr}$ values were calculated from measured $\varepsilon^{180}Hf$ and $\varepsilon^{178}Hf$ values using equation (4). The $\varepsilon^{149}Sm$ values are from ref. 35 Error ellipses represent the 95% confidence intervals. Also shown are predicted isotopic variations at different neutron fluence conditions. The dashed and dotted lines are loci of equal neutron fluences of thermal (Φ) and epithermal (Θ) neutrons, respectively.

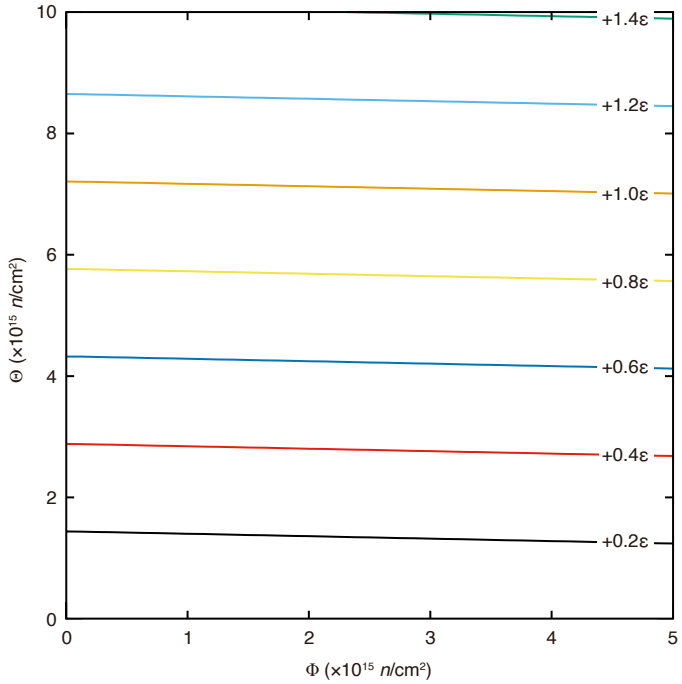

Extended Data Fig. 2 | Excess ^{176}Hf produced by reactions with cosmogenic neutrons. Contours of ^{176}Hf/^{177}Hf shifts arising from neutron-induced reactions are plotted as a function of thermal (Φ) and epithermal (Θ) neutron fluences. The contour interval is 0.2ε.

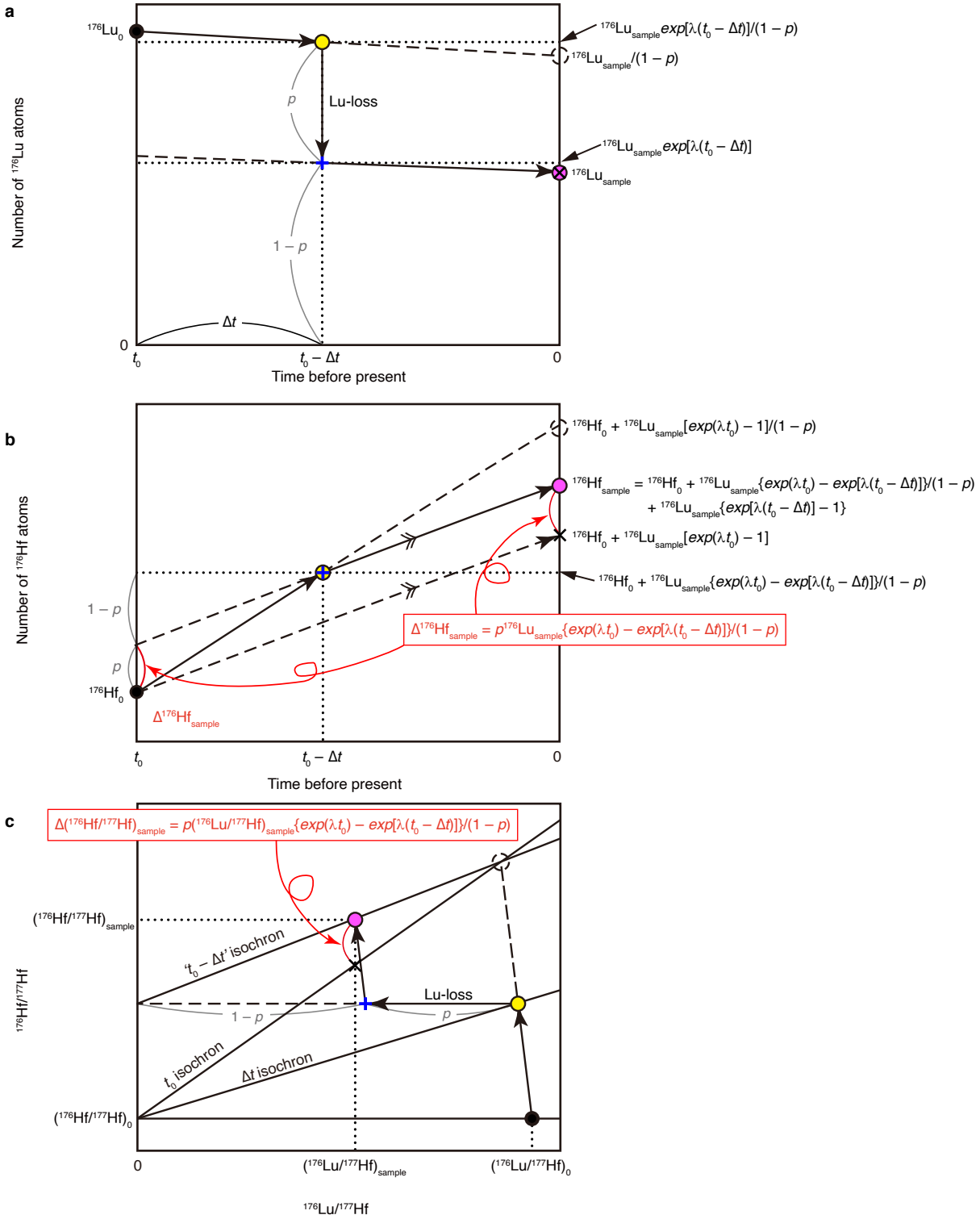

Extended Data Fig. 3 | Schematics of the Lu–Hf isotopic evolution of an object subjected to secondary Lu-loss. We consider the case in which the object formed at t_0 and lost Lu with a proportion p at a time Δt after the formation. **a**. Radioactive decay and loss of ^{176}Lu. **b**. Radiogenic growth of ^{176}Hf. **c**. ^{176}Hf/^{177}Hf versus ^{176}Lu/^{177}Hf isochron diagram. Subscripts '0' and 'sample' refer to the initial (at t_0) and present values in the object, respectively. Notation is the same as equation (1). The $(^{176}Hf/^{177}Hf)_0$ value of the object can be regarded as the same as the meteorite zircon value[30]. The degree of apparent ^{176}Hf excess ($\Delta^{176}Hf_{sample}$) is a function of the extent (p) and timing (Δt) of Lu-loss.

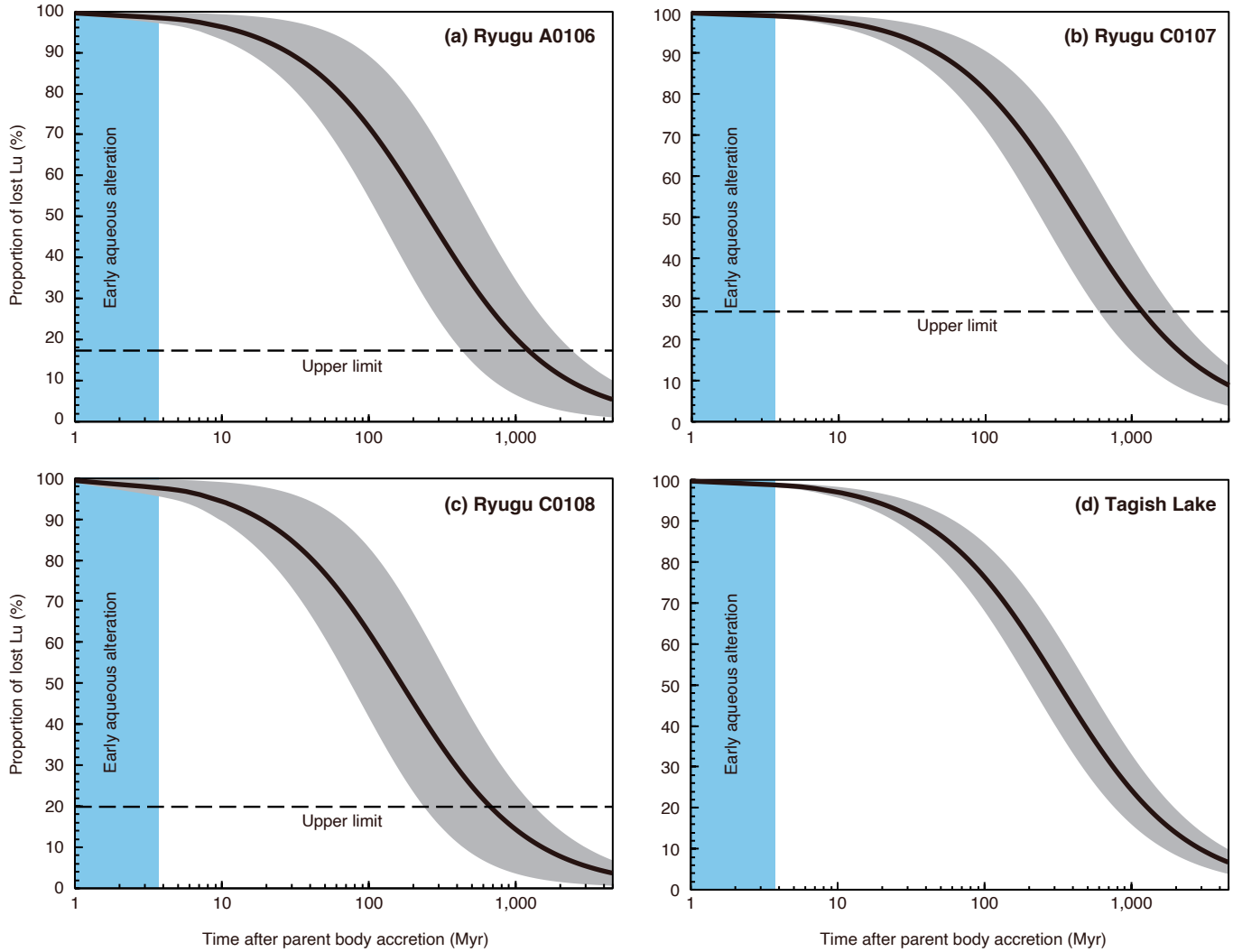

Extended Data Fig. 4 | Timing and extent of Lu-loss to produce apparent excess ^{176}Hf. The Ryugu samples A0106 (**a**), C0107 (**b**), and C0108 (**c**) and the ungrouped carbonaceous chondrite Tagish Lake (**d**). Notation is the same as in Fig. 3. For Ryugu samples, the upper limits on the proportion of lost Lu are estimated to be 14–27%, and the resultant lower bounds on the interval between the parent body accretion and Lu-loss are 10^3 Myr.

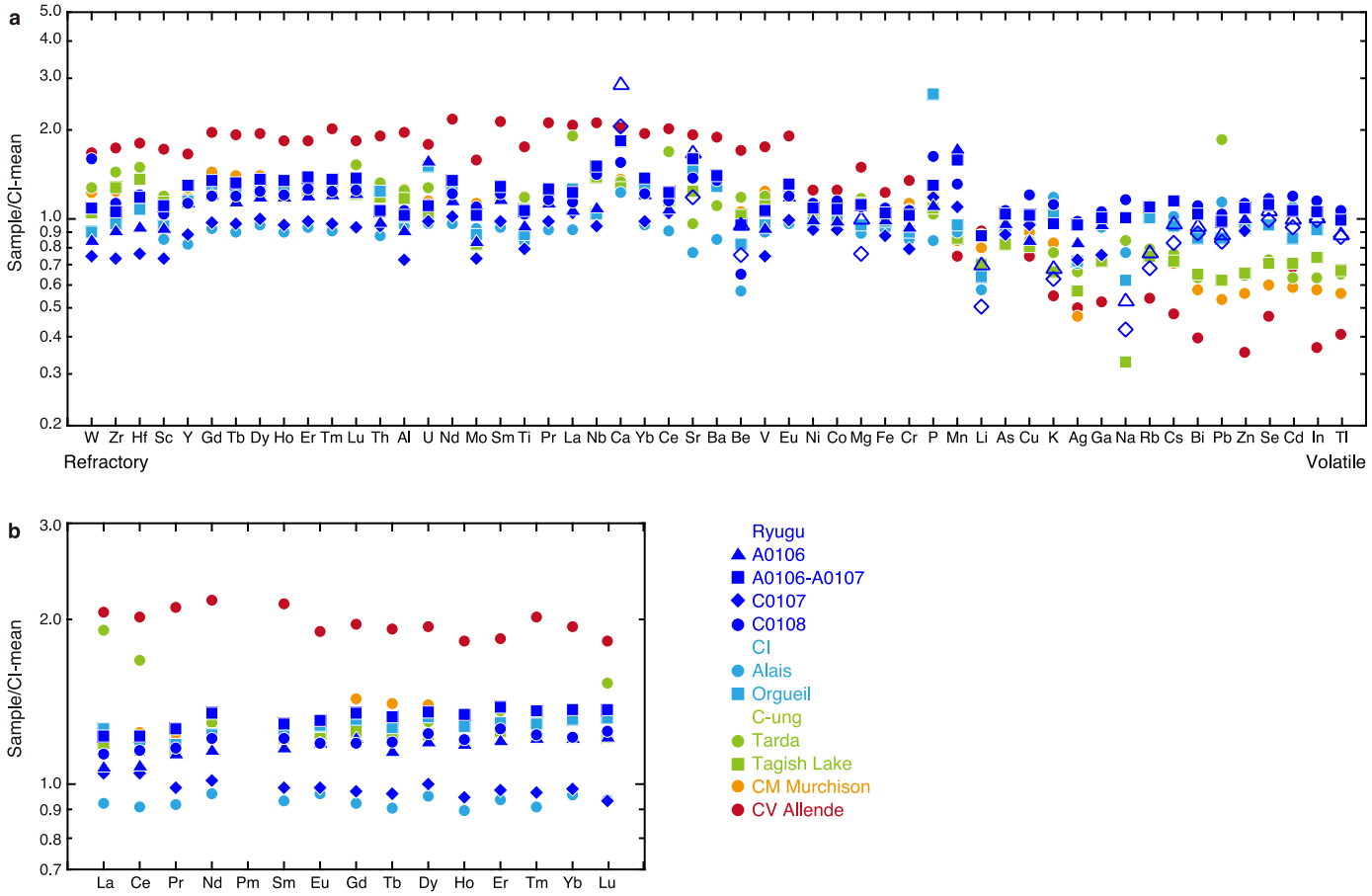

Extended Data Fig. 5 | Elemental abundance patterns of Ryugu and carbonaceous chondrite samples. a. Elemental abundances normalized to the CI chondrite mean values[80] are plotted on a log scale as a function of 50% condensation temperature[110]. For the SOM-extracted Ryugu samples A0106 and C0107, open symbols represent elements for which total yields of the SOM-extraction test using carbonaceous chondrites exceed 5% (Extended Data Table 3). The depletion of alkali elements in these samples compared to the pristine Ryugu samples A0106-A0107 and C0108 can be attributed to their leaching out with SOM, especially by water. **b.** REE abundances normalized to the CI chondrite mean values are plotted on a log scale in order of atomic number. For both **a** and **b**, the data for A0106-A0107 and C0108 are from ref. 9. The data from this work are listed in Extended Data Table 4.

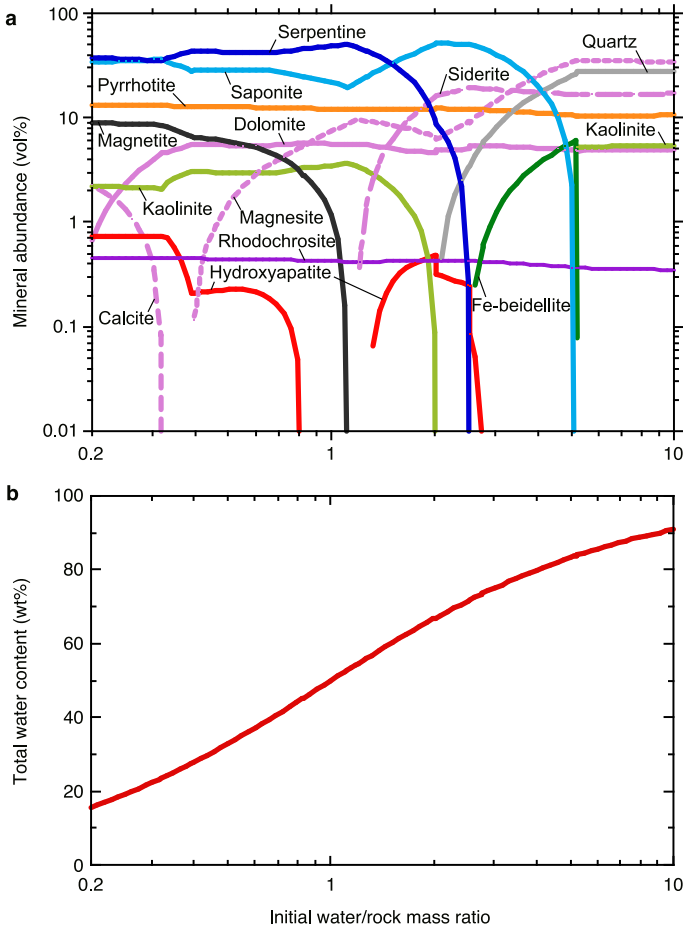

Extended Data Fig. 6 | Thermodynamic modeling of the aqueous alteration on the Ryugu parent body. The volume fractions of minerals in the rock (**a**) and the mass fraction of water in the rock-fluid system (**b**) are plotted as a function of initial water/rock mass ratio.

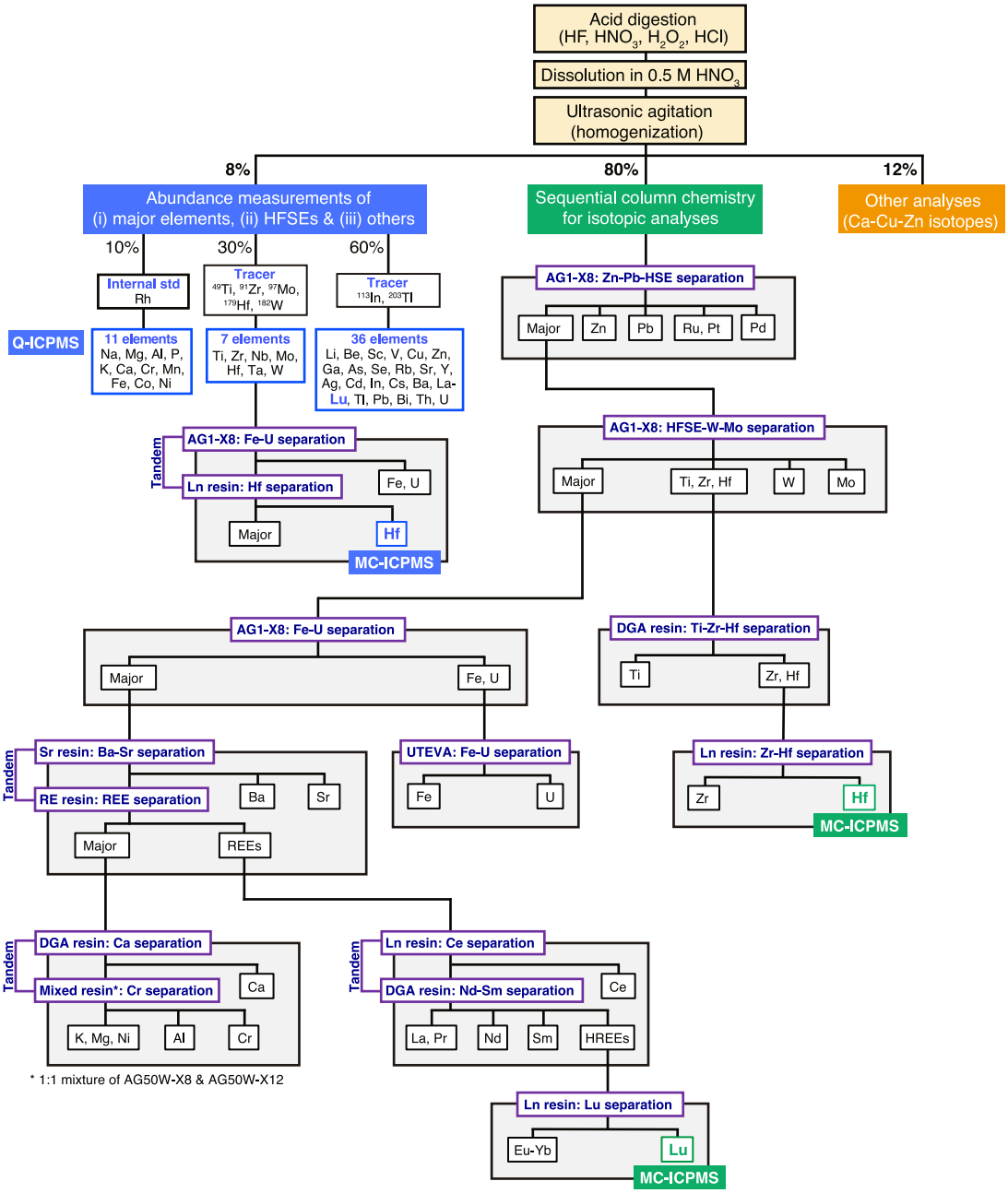

Extended Data Fig. 7 | A flowchart of series of sample processing by the Hayabusa2-initial-analysis chemistry team. These chemical processes were applied for chemical and isotopic analyses of Ryugu and carbonaceous samples.

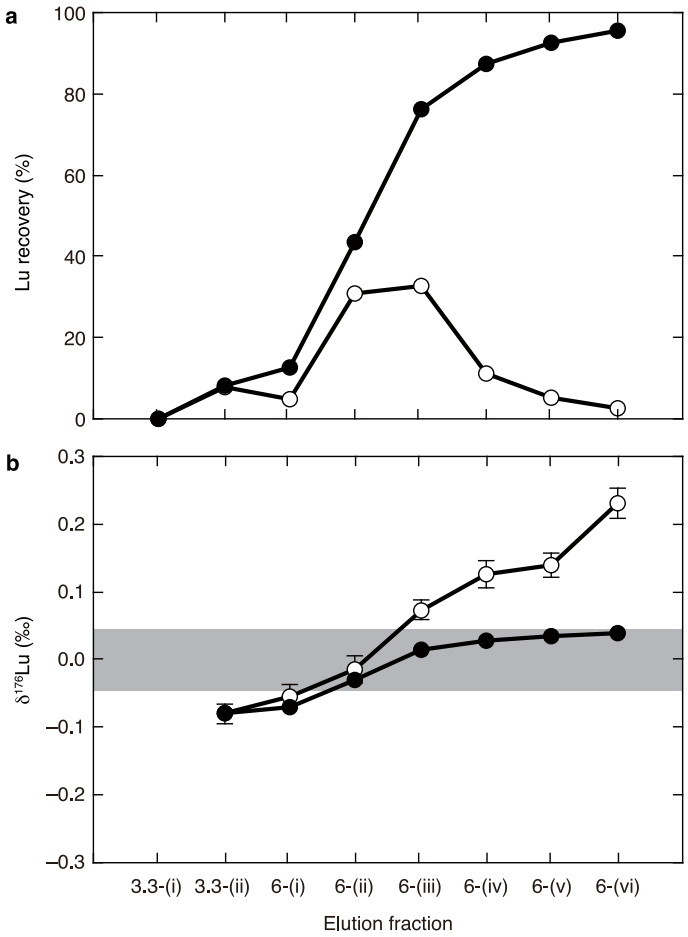

Extended Data Fig. 8 | Lu isotope fractionation induced by Ln resin chromatography. (a) Elution profile for Lu during the isotope fractionation experiment using the SPEX Lu standard solution. (**b)** Isotope composition of eluted Lu represented as δ^{176}Lu with respect to the unprocessed standard. Open symbols represent data for individual elution fractions, whereas solid symbols show those for the cumulative elution fractions. Error bars plotted on δ^{176}Lu for individual fractions represent the 2 s.e. internal precisions. Grey band expresses the 2 s.d. external reproducibility of analyses (n = 14) of the unprocessed standard. Elution fractions are as follow: 3.3-(i), the first elution with 14 mL of 3.3 M HCl; 3.3-(ii), the second elution with 4 mL of 3.3 M HCl; 6-(i) to 6-(V), the following successive elution sections with 0.5 mL of 6 M HCl; and 6-(vi), the last fraction eluted between 2.5 and 4.5 mL of 6 M HCl. The δ^{176}Lu values changed from negative at early elution stages to positive at late elution stages. The observed variation is comparable to analytical uncertainties for Ryugu samples and an order of magnitude smaller than required to account for the observed ^{176}Hf excesses by accelerated ^{176}Lu decay.

Extended Data Table 1 | Lu–Hf isotopic data for Ryugu and carbonaceous chondrite samples

Sample	Sample weight		Hf*	$^{176}Lu/^{177}Hf$†	$^{176}Hf/^{177}Hf$§	$\Delta(^{176}Hf/^{177}Hf)$	$\varepsilon^{174}Hf$§	$\varepsilon^{178}Hf$§	$\varepsilon^{180}Hf$§	Correlation factors		$\varepsilon^{178}Hf_{corr}$	$(^{176}Hf/^{177}Hf)_{corr}$	$\Delta(^{176}Hf/^{177}Hf)_{corr}$
	Powdering	Analysis	(μg/g)							180-178	180-176			
Ryugu														
A0106	17.15	17.15	0.1027 ± 0.0039	0.0422 ± 0.0019	0.283761 ± 0.000020	0.00023 ± 0.00017	7 ± 20	0.11 ± 0.30	0.13 ± 0.48	0.21	-0.14	0.00 ± 0.19		
A0106-A0107	28.89	23.88	0.1186 ± 0.0016	0.0409 ± 0.0015	0.283580 ± 0.000017	0.00017 ± 0.00013	11 ± 14	-0.17 ± 0.23	-0.52 ± 0.37	0.27	-0.33	0.11 ± 0.14	0.283618 ± 0.000036	0.00021 ± 0.00014
C0107	17.36	17.36	0.0810 ± 0.0036	0.0408 ± 0.0021	0.283802 ± 0.000022	0.00040 ± 0.00019	1 ± 28	0.92 ± 0.25	0.65 ± 0.52	0.15	-0.28	0.16 ± 0.20	0.283754 ± 0.000049	0.00035 ± 0.00020
C0108	33.34	22.24	0.1243 ± 0.0016	0.0356 ± 0.0011	0.283022 ± 0.000013	0.00008 ± 0.00010	9 ± 11	-0.21 ± 0.21	-0.61 ± 0.36	0.23	-0.21	0.13 ± 0.14	0.283066 ± 0.000032	0.00012 ± 0.00010
Carbonaceous Chondrites														
Orgueil (CI)	50	20.82	0.1096 ± 0.0016	0.0426 ± 0.0009	0.283558 ± 0.000020	-0.00001 ± 0.00008	10 ± 22	-0.24 ± 0.26	-0.38 ± 0.52	0.28	-0.23	0.03 ± 0.19		
Alais (CI)	51	21.98	0.1053 ± 0.0016	0.0315 ± 0.0012	0.282683 ± 0.000027	0.00010 ± 0.00011	-5 ± 28	0.22 ± 0.35	0.00 ± 0.58	0.24	-0.44	0.10 ± 0.23		
Tagish Lake (C-ung)	1055	24.29	0.1403 ± 0.0017	0.0307 ± 0.0008	0.282658 ± 0.000022	0.00015 ± 0.00008	5 ± 17	-0.26 ± 0.26	-0.73 ± 0.42	0.28	-0.41	0.15 ± 0.16	0.282711 ± 0.000044	0.00020 ± 0.00009
Tarda (C-ung)	212	25.10	0.1596 ± 0.0016	0.0339 ± 0.0006	0.282780 ± 0.000012	-0.00001 ± 0.00005	-1 ± 18	-0.43 ± 0.23	-0.96 ± 0.44	0.44	-0.26	0.16 ± 0.14	0.282849 ± 0.000037	0.00006 ± 0.00006
Murchison (CM)	1645	24.76	0.1384 ± 0.0017	0.0343 ± 0.0007	0.282791 ± 0.000016	-0.00003 ± 0.00006	-12 ± 15	-0.04 ± 0.20	-0.27 ± 0.37	0.23	-0.27	0.08 ± 0.14		
Allende (CV)	4 kg	24.92	0.1888 ± 0.0021	0.0342 ± 0.0007	0.282822 ± 0.000015	0.00000 ± 0.00007	6 ± 16	0.05 ± 0.23	0.00 ± 0.34	0.42	-0.13	0.02 ± 0.12		

Sample weights are in mg unless otherwise stated. The Lu abundance data for A0106-A0107 and C0108 are from ref. 9 Subscript 'corr' refers to corrected for nucleosynthetic effects.

*Errors on Hf abundances include uncertainties in measured $^{179}Hf/^{178}Hf$, tracer composition, and blank amount.

†Errors on $^{176}Lu/^{177}Hf$ values combine the errors on the Hf and Lu abundances in quadrature.

§Errors on Hf isotopic ratios combine the 2 s.e. internal precisions and the 2 s.d. reproducibilities of the bracketing JMC-Hf 475 standard runs, added in quadrature.

Extended Data Table 2 | Lu isotopic data for Ryugu and carbonaceous chondrite samples

Sample	δ^{176}Lu
Ryugu	
A0106	-0.39 ± 0.23
A0106-0107	-0.13 ± 0.19
C0107	-0.29 ± 0.23
C0108	0.04 ± 0.20
Carbonaceous Chondrite	
Orgueil (CI1)	-0.07 ± 0.20
Allende (CV3)	0.03 ± 0.23

Errors combine the 2 s.e. internal precisions and the 2 s.d. external reproducibilities of the bracketing standard runs, added in quadrature.

Extended Data Table 3 | Recovery yields of elements during the four-step SOM extraction

	Orgueil					Tarda				
Yield (%)	Hexane	DCM	MeOH	H_2O	Total	Hexane	DCM	MeOH	H_2O	Total
Li	b.d.l	b.d.l.	b.d.l.	1.94	1.94	0.23	0.22	1.50	6.57	8.51
Be	0.88	0.24	0.11	10.0	11.3	0.06	0.21	0.59	2.40	3.26
Na	0.18	0.31	21.4	72.3	94.1	0.34	0.21	32.8	44.2	77.5
Mg	0.03	0.13	4.47	7.79	12.4	0.04	0.12	1.12	1.72	3.00
Al	0.02	0.18	0.05	0.32	0.57	0.04	0.13	0.71	0.47	1.35
P	0.03	0.11	0.04	0.29	0.47	0.04	0.13	0.18	0.42	0.77
K	0.20	0.37	1.76	65.6	67.9	0.63	0.32	3.14	50.1	54.2
Ca	0.28	0.21	0.38	37.9	38.8	0.04	0.09	0.18	7.14	7.45
Sc	5.09	0.22	0.09	0.95	6.35	0.06	0.21	1.78	1.09	3.14
Ti	0.02	0.08	0.02	0.18	0.30	0.03	0.09	0.48	0.31	0.91
V	0.02	0.12	0.07	0.28	0.49	0.03	0.11	0.62	0.32	1.09
Cr	0.01	0.10	0.04	0.24	0.39	0.03	0.11	0.53	0.32	0.99
Mn	0.03	0.12	1.43	4.57	6.14	0.03	0.09	0.30	0.33	0.75
Fe	0.01	0.10	0.04	0.26	0.42	0.03	0.09	0.32	0.30	0.73
Co	0.02	0.11	0.11	0.40	0.64	0.03	0.10	0.24	0.36	0.74
Ni	0.02	0.12	0.26	1.02	1.42	0.03	0.11	0.30	0.42	0.87
Cu	0.02	0.12	0.31	0.30	0.75	0.06	0.15	0.66	0.50	1.37
Zn	0.03	0.11	0.12	0.32	0.58	0.06	0.35	0.96	0.62	1.99
Ga	0.02	0.13	0.05	0.34	0.55	0.04	0.13	0.67	0.47	1.31
As	0.03	0.14	0.13	0.49	0.78	0.05	0.12	0.66	0.50	1.32
Se	0.25	0.16	3.67	14.3	18.4	0.05	0.15	0.72	0.80	1.72
Rb	0.11	0.12	0.54	64.8	65.6	0.05	0.13	0.69	28.4	29.2
Sr	0.24	1.00	2.59	33.1	36.9	0.09	0.14	1.31	13.1	14.6
Y	0.03	0.12	0.06	0.50	0.70	0.03	0.11	0.14	0.42	0.70
Zr	0.02	0.09	0.00	0.20	0.31	0.06	0.05	0.37	0.30	0.78
Nb	0.02	0.07	0.02	0.19	0.29	0.02	0.07	0.48	0.35	0.93
Ag	0.09	1.34	0.28	0.27	1.98	0.01	0.17	0.29	0.39	0.86
Cd	0.13	0.58	1.61	7.74	10.1	1.99	0.56	3.43	2.31	8.28
In	0.68	0.42	0.22	0.42	1.75	0.28	0.32	0.77	1.35	2.72
Cs	0.05	0.12	0.14	20.6	20.9	0.04	0.13	0.39	5.09	5.66
La	0.04	0.28	0.11	1.11	1.54	0.03	0.10	0.18	0.48	0.79
Ce	0.03	0.23	0.07	0.82	1.15	0.03	0.10	0.18	0.43	0.75
Pr	0.06	0.21	0.07	0.67	1.02	0.02	0.10	0.16	0.43	0.71
Nd	0.04	0.18	0.06	0.63	0.91	0.03	0.11	0.18	0.38	0.70
Sm	0.03	0.15	0.04	0.53	0.76	0.04	0.09	0.18	0.39	0.70
Eu	0.07	0.20	0.59	3.28	4.14	0.03	0.12	0.49	1.59	2.23
Gd	0.04	0.13	0.07	0.51	0.76	0.03	0.12	0.16	0.42	0.73
Tb	0.13	0.18	0.10	0.45	0.87	0.06	0.15	0.19	0.42	0.82
Dy	0.04	0.13	0.05	0.43	0.64	0.03	0.11	0.13	0.40	0.66
Ho	0.09	0.17	0.07	0.46	0.78	0.03	0.11	0.15	0.46	0.75
Er	0.05	0.14	0.06	0.52	0.77	0.03	0.12	0.14	0.45	0.74
Tm	0.15	0.22	0.10	0.55	1.02	0.03	0.12	0.17	0.49	0.81
Yb	0.04	0.12	0.05	0.51	0.72	0.02	0.10	0.19	0.47	0.79
Lu	0.13	0.18	0.09	0.60	0.99	0.03	0.10	0.22	0.48	0.83
Hf	0.09	0.13	0.02	0.27	0.51	0.06	0.09	0.54	0.34	1.04
Ta	0.23	0.21	0.11	0.62	1.17	0.04	0.12	0.80	0.27	1.23
W	0.56	0.52	0.37	1.40	2.85	0.09	0.13	0.38	0.81	1.41
Tl	0.07	0.09	0.19	12.8	13.1	0.01	0.16	0.31	0.51	0.99
Pb	0.07	0.25	0.15	0.65	1.12	0.36	0.12	0.24	0.32	1.04
Bi	3.56	1.96	2.74	18.5	26.7	10.6	4.13	6.92	30.5	52.2
Th	0.07	0.20	0.15	0.42	0.85	0.01	0.11	0.36	0.22	0.70
U	b.d.l.	0.25	0.59	5.53	6.37	0.00	0.04	0.36	1.11	1.51

b.d.l., below detection limit.

Extended Data Table 4 | Elemental abundance data for Ryugu and carbonaceous chondrite samples

	Abundance (μg/g)								Uncertainty (%)							
	A0106	C0107	Orgueil	Alais	Tagish Lake	Tarda	Murchison	Allende	A0106	C0107	Orgueil	Alais	Tagish Lake	Tarda	Murchison	Allende
Li	1.06	0.76	0.96	0.87	1.05	1.03	1.20	1.38	5.0	3.2	3.2	5.2	7.6	10.2	8.2	7.5
Be	0.021	0.017	0.018	0.013	0.023	0.0260	0.023	0.0376	24	20	10	33	25	6.2	11	6.8
Na	2720	2160	3180	3940	1680	4300	3180	3150	1.4	1.6	1.8	1.7	2.1	3.2	2.3	2.4
Mg	96200	72800	91200	84700	107000	111000	111000	142000	2.8	2.9	3.0	2.9	1.2	2.1	1.1	1.7
Al	7700	6080	8490	7880	9850	10500	10600	16400	0.9	1.2	1.3	1.1	1.8	2.6	1.6	1.9
P	1100	1150	2580	825	1060	1020	1170	1230	5.4	5.3	5.3	5.4	6.4	4.8	5.1	4.6
K	371	336	552	641	358	416	447	296	1.8	1.9	1.9	1.7	4.2	3.6	3.7	4.1
Ca	25500	18200	16000	10800	11300	11800	12000	18000	1.2	1.1	1.3	1.2	2.2	2.2	2.2	2.2
Sc	5.44	4.27	5.53	4.95	6.64	6.97	6.99	10.0	0.0	0.0	0.0	0.0	1.9	3.6	1.5	2.1
Ti	429	355	397	378	486	530	537	788	2.3	2.3	2.1	2.0	1.3	1.0	1.0	1.2
V	50.0	40.1	51.1	48.2	59.4	63.8	66.2	93.6	5.8	0.8	2.0	2.7	4.3	3.8	3.2	3.4
Cr	2470	2060	2360	2220	2750	2820	2940	3520	1.6	1.4	1.8	1.5	2.5	1.9	1.2	1.7
Mn	3290	2080	1810	1710	1630	1640	1600	1420	1.0	1.1	1.3	3.5	2.6	1.7	1.2	1.5
Fe	186000	163000	182000	170000	192000	199000	203000	228000	1.7	1.7	1.9	1.9	1.1	1.8	1.2	1.4
Co	503	467	500	503	525	546	566	638	1.1	1.1	1.2	1.2	1.2	1.2	1.3	1.2
Ni	11000	10000	10600	10300	11400	11800	12200	13700	1.1	1.3	1.3	1.5	1.2	1.6	1.2	1.6
Cu	111	124	131	127	105	110	117	97	1.2	0.9	1.0	1.1	2.8	3.4	2.6	2.8
Zn	314	282	288	298	204	201	174	110	1.4	1.5	1.3	1.1	2.6	3.2	2.5	2.8
Ga	9.14	7.12	9.56	8.86	6.78	6.78	6.89	4.98	1.5	2.2	1.3	1.7	4.1	4.9	4.2	4.9
As	1.73	1.56	1.62	1.67	1.46	1.51	1.70	1.54	3.0	3.6	4.5	4.5	3.7	3.1	3.9	3.6
Se	21.9	20.2	19.5	19.5	14.5	14.8	12.2	9.6	4.5	5.5	6.9	5.4	3.6	4.1	5.8	4.4
Rb	1.72	1.51	2.23	2.27	1.66	1.75	1.75	1.19	1.8	1.5	2.6	1.4	2.2	3.5	1.9	2.3
Sr	13.2	9.18	11.4	5.99	9.67	7.54	9.77	15.0	1.5	2.1	1.2	1.4	1.3	2.3	1.1	1.6
Y	1.71	1.33	1.72	1.23	1.69	1.92	1.78	2.49	1.6	1.4	1.0	1.3	1.4	2.1	1.7	1.2
Zr	3.48	2.78	3.64	3.64	4.83	5.46	4.72	6.60	1.9	4.3	4.6	1.8	2.2	1.8	1.4	1.9
Nb	0.305	0.263	0.288	0.265	0.386	0.420	0.407	0.592	2.5	6.4	4.8	4.2	3.0	3.0	3.4	1.7
Mo	0.82	0.72	0.86	0.90	0.80	1.01	1.11	1.54	2.0	1.6	2.1	2.5	1.2	1.8	1.3	1.8
Ag	0.171	0.148	0.147	0.145	0.117	0.135	0.096	0.102	2.4	10.7	8.4	9.0	8.6	6.1	7.9	8.3
Cd	0.688	0.635	0.583	0.746	0.482	0.428	0.398	0.466	4.7	4.4	4.4	4.5	3.0	4.7	4.7	4.3
In	0.080	0.078	0.073	0.074	0.058	0.050	0.045	0.029	10.9	7.1	6.6	6.5	4.3	4.3	7.7	20.1
Cs	0.184	0.155	0.177	0.192	0.136	0.144	0.133	0.089	3.4	1.9	1.9	2.8	2.8	2.6	3.4	3.3
Ba	n.d.	n.d.	3.08	2.05	3.09	2.65	3.29	4.53	n.d.	n.d.	1.6	1.2	2.5	2.2	1.9	2.3
La	0.264	0.255	0.309	0.225	0.290	0.467	0.302	0.505	2.4	2.0	1.6	1.9	1.5	1.8	1.7	1.8
Ce	0.680	0.657	0.759	0.571	0.724	1.05	0.779	1.27	2.7	2.7	2.4	2.4	1.3	2.2	1.3	1.3
Pr	0.109	0.094	0.113	0.087	0.110	0.120	0.118	0.200	2.0	2.3	2.4	3.2	1.8	1.4	1.9	2.0
Nd	0.547	0.481	0.583	0.455	0.585	0.612	0.624	1.02	2.1	1.8	1.9	3.1	1.4	1.7	2.2	1.4
Sm	0.180	0.151	0.192	0.143	0.186	0.197	0.197	0.328	3.7	2.1	4.7	2.8	2.6	4.0	2.9	1.4
Eu	0.0690	0.0569	0.0740	0.0555	0.0700	0.0725	0.0723	0.110	1.4	2.4	2.2	2.5	1.9	1.5	2.0	2.2
Gd	0.253	0.202	0.274	0.192	0.260	0.266	0.298	0.408	2.8	2.0	2.4	1.8	2.2	0.8	1.3	2.8
Tb	0.0439	0.0366	0.0482	0.0344	0.0468	0.0489	0.0534	0.0732	2.5	2.7	2.1	2.6	1.2	2.1	1.2	1.5
Dy	0.302	0.252	0.335	0.240	0.310	0.328	0.353	0.490	1.7	1.2	2.6	1.2	1.4	1.8	1.4	1.5
Ho	0.0670	0.0535	0.0719	0.0506	0.0669	0.0721	0.0719	0.1032	1.6	1.7	2.1	3.5	1.4	1.4	1.2	0.8
Er	0.199	0.160	0.213	0.154	0.205	0.224	0.211	0.303	2.3	2.1	1.6	1.9	1.3	1.3	2.4	2.3
Tm	0.0315	0.0250	0.0334	0.0235	0.0315	0.0326	0.0344	0.0525	1.5	2.5	2.3	3.1	2.1	1.7	1.9	1.9
Yb	0.204	0.164	0.219	0.160	0.203	0.218	0.221	0.324	2.3	1.5	1.9	1.8	1.5	1.1	1.2	2.2
Lu	0.0306	0.0233	0.0330	0.0234	0.0304	0.0381	0.0334	0.0456	2.5	2.8	1.5	3.4	2.4	1.3	1.5	1.7
Hf	0.100	0.081	0.115	0.117	0.145	0.158	0.143	0.191	5.6	9.6	3.0	10.5	4.8	2.5	4.5	3.3
Ta	0.094	0.101	0.019	0.018	0.020	0.022	0.021	0.033	3.4	3.3	4.2	2.7	2.6	3.0	1.4	2.5
W	0.087	0.076	0.092	0.090	0.107	0.130	0.125	0.171	5.3	2.5	5.2	7.9	2.9	2.0	5.4	2.7
Tl	0.126	0.122	0.143	0.146	0.095	0.092	0.079	0.057	2.3	4.3	1.8	3.8	4.1	6.8	5.5	7.5
Pb	2.36	2.22	2.28	3.00	1.64	4.89	1.40	2.60	1.9	1.5	1.8	1.4	3.6	3.7	3.5	3.5
Bi	0.108	0.101	0.098	0.102	0.074	0.071	0.065	0.045	2.3	1.8	3.4	2.2	3.5	4.2	3.9	4.7
Th	0.0293	0.0281	0.0369	0.0261	0.0353	0.0393	0.0383	0.0568	2.9	1.5	2.3	2.1	4.4	4.1	4.5	4.5
U	0.0129	0.0080	0.0123	0.0078	0.0084	0.0104	0.0094	0.0146	2.7	1.6	2.7	2.6	6.0	4.7	5.5	4.7

For the SOM-extracted Ryugu samples A0106 and C0107, elemental abundances were calculated using the sample weights before the SOM extraction. The measured abundances of elements for which total yields of the SOM-extraction test using carbonaceous chondrites exceed 5% (Extended Data Table 3) are shown in red. n.d., not determined due to contamination during the SOM extraction. Uncertainties represent the 95% confidence levels, which were estimated by propagating the 2 s.e. internal precisions of measurements and uncertainties of tracer composition.